59

Buoyancy-driven convection with a uniform magnetic field. Part 2. Experimental investigation

By L. DAVOUST[1]†, M. D. COWLEY[2], R. MOREAU[1]
AND R. BOLCATO[1]

[1]EPM-Madylam Laboratory, ENSHMG BP 95, 38402 St. Martin d'Hères, France
[2]Cambridge University Engineering Department, Cambridge CB2 1PZ, UK

In this paper, an experimental study of laminar magnetohydrodynamic (MHD) buoyancy-driven flow in a cylindrical cell with axis horizontal is described. A steady uniform magnetic field is applied vertically to the mercury-filled cell, which is also subjected to a horizontal temperature gradient. The main features of this internal MHD thermogravitational flow are made experimentally evident from temperature and electric potential measurements. Whatever the level of convection, raising the Hartmann number Ha to a value of the order of 10 is sufficient to stabilize an initially turbulent flow. At much higher values of the Hartmann number ($Ha \sim 100$) the MHD effects cause a change of regime from boundary-layer driven to core driven. In this latter regime an inviscid inertialess MHD core flow is bounded by a Hartmann layer on the horizontal cylindrical wall and viscous layers on the endwalls. Since the Hartmann layer is found to stay electrically inactive along the cell, the relevant asymptotic ($Ha \gg 1$) laws for velocity and heat transfer are found from the balance between the curl of buoyancy and Lorentz forces in the core, together with the condition that the flow of electric current between core and Hartmann layer is negligible. A modified Rayleigh number Ra_G/Ha^2, which is a measure of the ratio of thermal convection to diffusion when there is a balance between buoyancy and Lorentz forces, is the determining parameter for the flow.

1. Introduction

A technologically important solidification process is the growth of semi-conductor crystals from a melt. A dopant is usually introduced in the melt in order to give the appropriate electronic properties to the semi-conductor crystals so formed. Because density gradients occur, buoyancy-driven flows arise and it is well-known that they are responsible for major defects like macrosegregations or striations (Langlois 1985). In the case of the Bridgman crystal-growth technique, a closed crucible contains both solid and liquid phases, separated from each other by a solidification interface. For a vertical Bridgman furnace, where the melt stays in the upper part of the crucible, the axial temperature gradient is opposed to gravity and the flow tends therefore to be naturally stabilized. Nevertheless, any deformation of the solidification interface from the horizontal, which is *a priori* unpredictable, generates horizontal density gradients

† Present address: Laboratoire des Ecoulements Géophysiques et Industriels, BP 53, 38041 Grenoble cedex 9, France.

and induces a flow whose magnitude is strong enough to modify dramatically mass transfer of dopant. For liquid semi-conductors or liquid metals, the molecular viscosity is typically much larger than the chemical diffusivity (i.e. the Schmidt number is large), so that convection is important in this context. On the other hand, the horizontal Bridgman crystal-growth configuration, with an imposed axial temperature gradient gives rise naturally to a primary convective loop – the so-called Hadley circulation. This flow in the absence of electromagnetic effects has been modelled by Cormack, Leal & Imberger (1974).

Macrosegregation and striations are related to an undesirable level of convection and to hydrodynamical instabilities respectively. Their elimination – a goal in crystal growth – could be promoted by solidification in micro-gravity. However, the use of a steady magnetic field is more attainable, which is known to be an efficient tool for damping the buoyancy-driven flow in a horizontal Bridgman crystal-growth configuration (Utech & Flemings 1966). Normally the concentration of the dilute chemical species (including both the injected dopant and the chemical impurities) is small enough so that buoyancy is essentially due to temperature gradients alone. The Schmidt number is so large that the concentration field behaves as a passive scalar.

Since motion plays a key role, the study of how MHD effects influence the Hadley circulation in the horizontal Bridgman configuration is the aim of the present paper, which complements former purely theoretical papers (Garandet, Alboussière & Moreau 1992; Alboussière, Garandet & Moreau 1993, 1996) from the same group. Of these papers, the one by Alboussière *et al.* (1993) is particularly relevant and is the Part 1 to the present Part 2.

1.1. *Internal thermogravitational flows in the absence of MHD effects*

Ordinary internal thermogravitational flows (Bejan 1984) subjected to a *horizontal* temperature gradient always involve a primary vortical loop, the Hadley circulation, characterized mainly by a horizontal vorticity component $\boldsymbol{\Omega} = -\Omega\hat{\boldsymbol{y}}$, where the horizontal unit vector $\hat{\boldsymbol{y}}$ has the direction of the product $\boldsymbol{G} \times \boldsymbol{g}$, $\boldsymbol{G}$ and $\boldsymbol{g}$ designating respectively the core horizontal temperature gradient and gravitational acceleration. If buoyancy forces, upwards near the hot endwall and downwards near the cold endwall, are balanced by vertical pressure gradients, varying axial pressure gradients arise, which drive the Hadley circulation.

For internal thermogravitational flows of fluids with moderate to high Prandtl number (Pr), Bejan (1984) distinguished between three thermal regimes, *conduction dominated*, *core driven* and *boundary-layer driven*. Bejan's classification was defined in the context of two-dimensional enclosures, whereas we shall be concerned with cylindrical geometry, but the physical principles are similar and worth reviewing here. The regime that occurs depends on both the aspect ratio of the enclosure ε and the Rayleigh number Ra ($\varepsilon = h/l$ and $Ra = g\beta h^3 \Delta T/(\nu\alpha_d)$), where ν denotes the molecular viscosity, α_d thermal diffusivity, β the volumetric expansion coefficient, ΔT the temperature difference between the temperature T_2 of the hot endwall and the temperature T_1 of the cold endwall, h the height (vertical walls) and l the length (horizontal walls) of the enclosure (see figure 1).

Another difference from the conditions of Bejan's classification is that the present paper is concerned with low-Prandtl-number fluids (liquid metals). The former distinction between three thermal regimes still holds provided that the Boussinesq number, defined as the product of Pr and Ra, is treated as the new distinguishing parameter. When $Pr\,Ra \ll 1$, *conduction* dominates and the temperature distribution is given by a uniform gradient throughout the enclosure. The resulting buoyancy forces drive
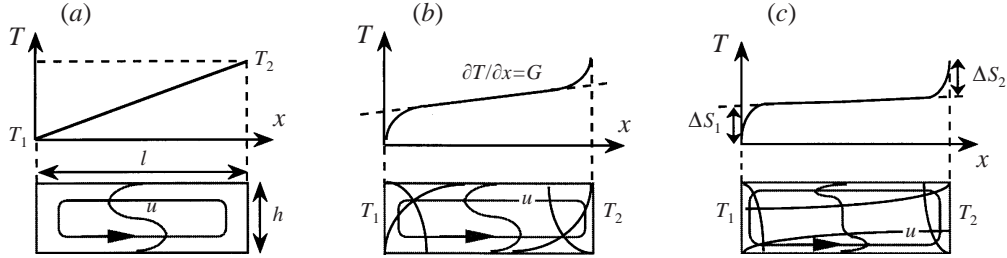
FIGURE 1. Three typical thermal regimes for aspect ratio $\varepsilon \ll 1$: (*a*) conduction dominated, $Pr\,Ra \ll 1$; (*b*) core-driven, $\varepsilon(Pr\,Ra)^{1/4} \ll 1$; (*c*) boundary-layer driven, $\varepsilon(Pr\,Ra)^{1/4} \gg 1$.

a small circulation, which takes the form of a fully developed flow, with horizontal velocity components only, over most of the length of the enclosure.

As the value of $Pr\,Ra$ is raised convection becomes important and the temperature distribution departs from that of a uniform gradient. If $\varepsilon(Pr\,Ra)^{1/4} < 1$, flow in the central region between the hot and cold ends may still be fully developed. However, there is now a convection component to the overall heat flux in that region, as well as the conduction associated with the temperature gradient. To match the overall flux to conduction at an endwall boundary, the temperature gradient must become steeper at the boundary. This steepening occurs in a boundary-layer thickness δ_t of order $h(Pr\,Ra)^{-1/4}$ and there are consequent 'temperature steps' at the endwalls (denoted on figure 1*c* by ΔS_1 and ΔS_2). If the longitudinal temperature gradient (denoted by G) is nearly the same as $(T_2 - T_1)/l$ (denoted by G_0), the end effects have a small influence on the overall behaviour and the situation is said to be *core driven*.

If $\varepsilon(Pr\,Ra)^{1/4} > 1$, end effects become dominant and the temperature distribution between the endwall boundary layers may approach a horizontally stratified condition. Flow is dictated by endwall conditions, there being insufficient length for vertical diffusion to produce a fully developed flow in the enclosure.

On figure 1, the typical thermal regimes – conduction dominated, core driven and boundary-layer driven – are sketched in the particular case of a small-aspect-ratio enclosure ($\varepsilon \ll 1$).

Finally, it should be noted that the Grashof number Gr defined as $g\beta h^3 \Delta T/v^2$, is relevant to the analysis of boundary-layer-driven regimes when inertia can no longer be neglected. Inertial end effects such as additional stationary loops are consistently observed for low-Prandtl-number fluids (Hart 1983) as Gr is increased.

1.2. *Damping of motion by means of a uniform magnetic field*

In this paper, we treat thermogravitational MHD flows for which convection of the magnetic field may be considered negligible (low magnetic Reynolds number). The Lorentz force which is due to the application of a steady uniform magnetic field $\boldsymbol{B}_0$ is responsible for a damping effect whose importance relative to viscous friction is given by the square of the magnitude of the Hartmann number Ha, defined as $Ha = \sqrt{\sigma/\rho v}\,B_0 h$. The symbol σ denotes the electric conductivity of the fluid. When the magnitude of the applied magnetic field $\boldsymbol{B}_0$ is sufficiently strong, a MHD reorganization of the flow is to be expected. Hartman layers (thickness Ha^{-1}) develop along walls which are not aligned with $\boldsymbol{B}_0$, and shear side layers (thickness $Ha^{-1/2}$) along walls parallel to $\boldsymbol{B}_0$. Viscous effects are confined to these layers, whereas the remainder of the flow – the MHD core flow – may be treated as inviscid.† As is the

† For simplicity in this introductory discussion, inertia effects are assumed negligible, but will be considered again in later sections.

case for pressure-driven flows (Hunt & Shercliff 1974), much care must be taken when calculating the velocity scale of such MHD internal thermogravitational flows. In particular, when the walls are electrically insulating, it is essential to adopt a three-dimensional point of view since the nature of the electric current path (resulting from the interaction between the velocity field and B_0) may dramatically modify the flow. If the current is forced to return via the Hartmann layers, the local core velocity is determined by the magnitude of the return current and the layer is said to be *active*. If electric current paths close themselves naturally within the MHD core flow, Hartmann layers are electrically inactive and the velocity scale is Ha^{-1} times that of the active condition. This active-layer case may occur when the cross-sectional shape of the horizontal enclosure is vertically asymmetric (Alboussière *et al.* 1993) or when the applied magnetic field B_0 is non-uniform and asymmetric about the horizontal central plane (Neubrand *et al.* 1995; Alboussière *et al.* 1996). The direction of the uniform applied magnetic field B_0 is also of the greatest importance. If B_0 is aligned with Ω, the velocity may scale as Ha^{-1} (Ozoe & Okada 1989; Ben Hadid & Henry 1997). In this last case, a two-dimensional flow is promoted within planes orthogonal to the direction of B_0 (Sommeria & Moreau 1982). Recently, a paper by Juel *et al.* (1998) has shown this tendency to bi-dimensionality well by the results of both numerical analysis and experiments.

The present paper focuses on the laminar MHD thermogravitational flow found in the apparatus with the acronym MASCOT, standing for MAgnetic Stabilization of COnvection and Turbulence. First, some guiding theoretical principles which directly support the experimental investigation of the flow are presented. It is found that the three flow regimes which occur in the absence of a magnetic field have their counterparts at high Hartmann number. Second, we describe the experimental convection cell and its instrumentation, which includes some novel sensors. Finally, experimental results taken from both local and global diagnostics of the flow are presented.

2. Theoretical background

The configuration to be studied is a horizontal circular cylinder whose aspect ratio ε (ratio of the radius r_0 to the length l) is small enough for a fully developed regime to be possible within the central core. The longitudinal cylindrical wall is supposed thermally insulating. Because of the centro-symmetric character of the laminar thermogravitational flow, the enclosure's geometry exhibits two planes of symmetry or skew-symmetry, namely the longitudinal vertical mid-plane XZ ($Y = 0$) and the transverse vertical mid-plane YZ ($X = 0$) as sketched on figure 2. The origin of the (X, Y, Z)-coordinate system is thus set at the centre point of the cylinder and these coordinates are also dimensionless, based on a scale length equal to the cylinder radius r_0 (the dimensional system (x, y, z) used later in the specification of the location of experimental measurements has its origin at the cold endwall). The imposed magnetic field B_0 is uniform and applied vertically. All walls are assumed to be perfect electrical insulators. The configuration is one in which the flow is efficiently damped since Hartmann layers stay electrically inactive and the Hadley vorticity Ω is perpendicular to B_0.

For the governing equations we adopt the Boussinesq approximation and non-dimensionalize variables on the basis that, with Hartmann layers inactive, current density is of order $\sigma u B_0$, where u is the horizontal velocity. A velocity scale u_0 is then provided by the assumption that there is a balance between buoyancy and Lorentz
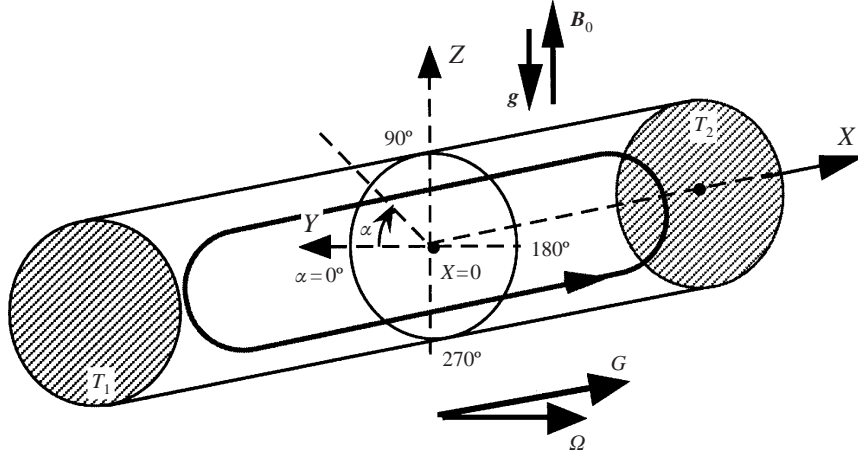
FIGURE 2. The configuration of MASCOT.

forces: $u_0 = \rho g \beta \, \Delta T / \sigma B_0^2$, where ΔT is a characteristic temperature difference. As in §1.1, ΔT might be taken as the overall temperature difference $T_2 - T_1$, but for much of the discussion a more appropriate value for ΔT is the longitudinal temperature difference within the core over a length equal to the cylinder radius r_0, i.e. $\Delta T = G \, r_0$ where G is the axial temperature gradient in the core. The value of G may reach its asymptotic level $G_0 = (T_2 - T_1)/l$ when a pure *conduction* regime is achieved. Taking other scales as $\sigma u_0 B_0^2 r_0$ for pressure, $\sigma u_0 B_0$ for current density and $u_0 B_0 r_0$ for electric potential we obtain the following dimensionless set of equations, expressing continuity (1), the Navier–Stokes equations in the Boussinesq approximation (2), electric current conservation (3), Ohm's law (4) and the energy equation (5):

$$\nabla \cdot U = 0, \tag{1}$$

$$\frac{Gr}{Ha^4}(U \cdot \nabla U) = -\nabla P + \Theta \hat{z} + J \times \hat{z} + \frac{1}{Ha^4}\Delta U, \tag{2}$$

$$\nabla \cdot J = 0, \tag{3}$$

$$J = -\nabla \Phi + U \times \hat{z}, \tag{4}$$

$$\frac{Pr \, Gr}{Ha^2}(U \cdot \nabla \Theta) = \Delta \Theta. \tag{5}$$

The symbols U, P, J, Θ, Φ, Δ and $\hat{z}$ denote, respectively, the non-dimensional velocity, pressure, electric current density, temperature, electric potential, Laplacian operator and vertical unit vector.

Three non-dimensional groups appear in the set of equations: the Grashof number Gr, the Hartmann number Ha and the Prandtl number Pr in the following forms:

$$Gr = \frac{\beta g \, \Delta T \, r_0^3}{\nu^2}, \quad Ha = \sqrt{\frac{\sigma}{\rho \nu}} B_0 \, r_0, \quad Pr = \frac{\nu}{\alpha_d}, \tag{6}$$

where the vertical length scale h initially introduced in §1.1 has been replaced here by r_0. The combination of these groups seen in equation (5) will be found to have particular significance and will be referred to here as the modified Rayleigh number,

$$\frac{Ra}{Ha^2} = \frac{Pr \, Gr}{Ha^2}, \tag{7}$$

since it represents the ratio of convection to diffusion of temperature if the velocity is set by a balance between the curl of buoyancy and Lorentz forces, rather than buoyancy and viscous forces.

2.1. *Conduction-dominated regime*

With conduction dominant, the convection term of equation (5) must, by definition, be negligible, i.e. $Ra/Ha^2 \rightarrow 0$. Here, it is worth recalling that the temperature distribution takes the form of a uniform horizontal gradient G_0; the appropriate scale for the characteristic temperature ΔT is the temperature difference across a non-dimensional horizontal distance of unity, i.e. $\Delta T = G_0 r_0 = (T_2 - T_1)r_0/l$ and $\partial\Theta/\partial X = 1$. For this regime of pure conduction, Garandet *et al.* (1992) studied the two-dimensional analogue of the MASCOT geometry and found that for $Ha \gg 1$ the flow field consists of an inviscid, inertialess core, bounded by Hartmann layers on the horizontal walls and viscous layers of thickness $Ha^{-1/2}$ on the vertical endwalls. (It is easily shown that inertia may be neglected in the endwall layers provided $Ha^{2.5} \gg Gr$.)

Taking the curl of equation (2) to eliminate the pressure term and of equation (4) to eliminate the electric potential yields the set of equations for the core:

$$(\hat{z} \cdot \nabla)\boldsymbol{J} = \hat{z} \times \nabla\Theta, \tag{8}$$

$$(\hat{z} \cdot \nabla)\boldsymbol{U} = \nabla \times \boldsymbol{J}. \tag{9}$$

The solution for the two-dimensional analogue is therefore $J_Y = Z$, $U_X = -Z$. The flow is one of uniform shear along the length of the core and it may be regarded as being in a fully developed condition, as found by Garandet *et al.* (1992).

The first analytical study of enclosures of finite extent in the Y-direction, which therefore has to treat explicitly the return path of the electric current, was given in Part 1 (Alboussiere *et al.* 1993). Fully developed flows in cylinders of arbitrary cross-section were asymptotically modelled ($Ha \gg 1$), assuming a conduction-dominated regime. By the expression fully developed flow, we mean that the flow exhibits no variation in the axial direction ($\partial U/\partial X \equiv 0$). For a circular cross-section limited by an electrically insulating wall, as in the configuration of interest here, the solution of equations (8) and (9) with uniform temperature gradient, $\partial\Theta/\partial X = 1$, is

$$J_Y = Z, \quad J_Z = -Y, \quad U_X = -2Z. \tag{10}$$

The solution has been chosen to satisfy the condition that the Hartmann layers are inactive and therefore that electric current is returned within the core. In fact, the electric current lines are circles centred on the cylinder axis. However, an electric potential field appears in order to overcome electrical resistance to current flow in the vertical direction and Ohm's law (4) yields

$$\Phi = YZ. \tag{11}$$

It follows that $\boldsymbol{u} \times \boldsymbol{B}$ has to balance a potential gradient in the Y-direction as well as electrical resistance and, as given in equation (10), the flow field is one of uniform shear again, but twice as strong as that of the two-dimensional analogue.

The present authors do not know of any attempt at an analytical conduction-dominated solution for endwall viscous layers in the cylindrical case. Ben Hadid & Henry (1996) provided a computational solution for the cylinder as a whole (aspect ratio $r_0/l = 0.25$), but their plots of velocity and current density vectors have insufficient resolution to provide unequivocal insight into endwall flow. Some further analysis of the flow was provided by the numerical work of Davoust *et al.*

(1997) but it is not wholly conclusive since, here again, separate contributions of convection and conduction of temperature to the subsequent flow were not isolated. However, it is surmised here that, although there are important differences between the cylindrical case and its two-dimensional analogue (such as the appearance of velocity components in the Y-direction), the viscous layer of the latter will have its counterpart in the former. The fully developed flow will fill the length of the cell except in end layers of thickness $O(Ha^{-1/2})$, where the flow is returned.

2.2. *Fully developed flow*

When convection of temperature can no longer be neglected, it is expected that isotherms will tend to be swept towards the cold end of the cell in the upper half of the cylinder and towards the hot end in the lower half. Vertical temperature gradients are thereby introduced, but the temperature distribution will be subject to the condition that the cylinder wall is adiabatic, i.e. $\partial\Theta/\partial R = 0$ there.

If a fully developed condition is closely approached over some length near the central region of the cell, we may take the axial temperature gradient there, G, as constant. As suggested previously, it is convenient to take the dimensional temperature scale ΔT as this axial temperature gradient times the length scale. Thus, to distinguish the Grashof and modified Rayleigh numbers based on $\Delta T = G\, r_0$, they will be denoted by Gr_G and Ra_G/Ha^2.

Inspection of equations (8) and (9) for the current density and velocity in the core, together with equation (5) for temperature shows that the axial velocity and the Y- and Z-components of current density are decoupled from the influence of the temperature variation with Y and Z and any transverse, secondary, flow which may be induced by it. Equations (10) still give the primary current and flow solution, so that we may write

$$U = -2Z\hat{x} + U_s(Y,Z), \quad \Theta = X + \Theta_s(Y,Z), \tag{12}$$

where the secondary-flow velocity U_s has no X-component. The temperature equation then takes the form

$$\frac{\partial\Theta_s^2}{\partial Y^2} + \frac{\partial\Theta_s^2}{\partial Z^2} = \frac{Ra_G}{Ha^2}\left\{-2Z + U_{sy}\frac{\partial\Theta_s}{\partial Y} + U_{sz}\frac{\partial\Theta_s}{\partial Z}\right\}. \tag{13}$$

The fully developed condition implies that the longitudinal gradient of electric potential, $\partial\Phi/\partial X$, must be constant. Integration of the longitudinal component of Ohm's law (4) over the cross-section of the cylinder then shows that the constant is zero since there is no net longitudinal current. Introducing a stream function Ψ_s for the secondary flow, such that $U_{sy} = \partial\Psi_s/\partial Z$, equations (4) and (8) yield

$$\frac{\partial^2\Psi_s}{\partial Z^2} = -\frac{\partial\Theta_s}{\partial Y}. \tag{14}$$

A simple approach to the solution of equations (13) and (14) is to develop it using a power series in the modified Rayleigh number Ra_G/Ha^2 (Cowley 1995):

$$\Theta_s = \frac{Ra_G}{Ha^2}\Theta_1 + \left(\frac{Ra_G}{Ha^2}\right)^2\Theta_2 + \cdots,$$

$$\Psi_s = \frac{Ra_G}{Ha^2}\Psi_1 + \left(\frac{Ra_G}{Ha^2}\right)^2\Psi_2 + \cdots.$$
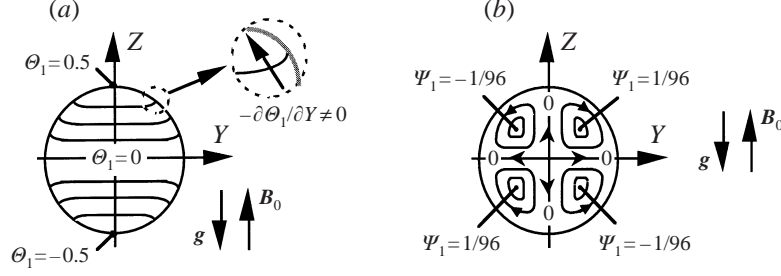
FIGURE 3. (a) Isotherms of the first-order temperature field Θ_1 and (b) streamlines of the resulting secondary transverse flow Ψ_1.

Equating terms of order Ra_G/Ha^2 yields after some algebra

$$\Theta_1 = \tfrac{1}{4}Z(3 - Y^2 - Z^2) = \tfrac{1}{4}R(3 - R^2)\sin\alpha, \tag{15}$$

$$\Psi_1 = \tfrac{1}{12}YZ(Y^2 + Z^2 - 1) = \tfrac{1}{24}R^2(R^2 - 1)\sin 2\alpha, \tag{16}$$

where (R, α) are cylindrical polar coordinates with α measured from the horizontal direction (see figure 2). According to equation (16) the secondary flow takes the quadripolar form of four vortices, each of them being located in a quadrant of the cross-section, as illustrated on figure 3(b). Figure 3 also shows how the adiabatic-wall condition forces a horizontal temperature gradient, which in turn drives the flow.

Measurement of temperature provides an important diagnostic tool in the investigation of physical behaviour in the cell. It is therefore of interest to obtain a feel for the value of Ra_G/Ha^2 below which the first-order solution of equation (15) provides a satisfactory approximation to Θ_s. Since the zero-order primary flow and temperature gradient are longitudinal, the second-order terms in the series expansion are zero. At third order, we obtain

$$\frac{1}{R}\frac{\partial}{\partial R}\left(R\frac{\partial \Theta_3}{\partial R}\right) + \frac{1}{R^2}\frac{\partial^2 \Theta_3}{\partial \alpha^2} = \frac{1}{R}\frac{\partial \Psi_1}{\partial R}\frac{\partial \Theta_1}{\partial R} - \frac{1}{R}\frac{\partial \Psi_1}{\partial R}\frac{\partial \Theta_1}{\partial \alpha},$$

and it is clear from the expressions for Θ_1 and Ψ_1 in equations (15) and (16) that the solution includes terms in $\sin\alpha$ and $\sin 3\alpha$ for the α-dependence. After some algebra it is found that the full solution for the temperature at the wall Θ_s up to third order in Ra_G/Ha^2 can be written

$$\Theta_s(R = 1, \alpha) = \frac{Ra_G}{Ha^2}\left\{\frac{1}{2}\sin\alpha\right\} + \left(\frac{Ra_G}{Ha^2}\right)^3\left\{\frac{7}{5850}\sin\alpha + \frac{1}{640}\sin\alpha\cos 2\alpha\right\}. \tag{17}$$

The lines of constant Θ_3 for the solution are given in figure 4.

It seems from equation (17) that the solution to first order should provide a satisfactory approximation up to quite moderate values of Ra_G/Ha^2. The robustness of the first-order result is further confirmed by the theory given in the Appendix for a fully developed flow when $Ha \gg Ra_G/Ha^2 \gg 1$. Under these conditions, the temperature variation in the Y-direction is confined to thermal layers of thickness order $(Ra_G/Ha^2)^{-1}$, as illustrated in figure 5. The central region forms a core in which the vertical gradient of Θ_s is of order Ra_G/Ha^2, while $\partial\Theta/\partial X$ is still taken to be unity, i.e. the core is near to being a thermally stratified region.
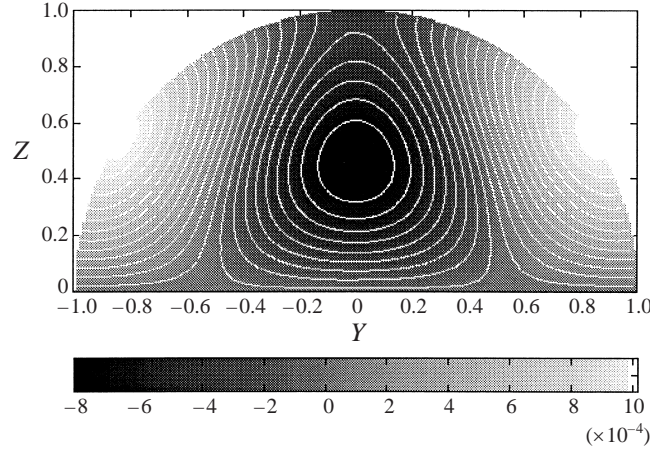
FIGURE 4. Third-order temperature term Θ_3 within the upper half of the cross-section.
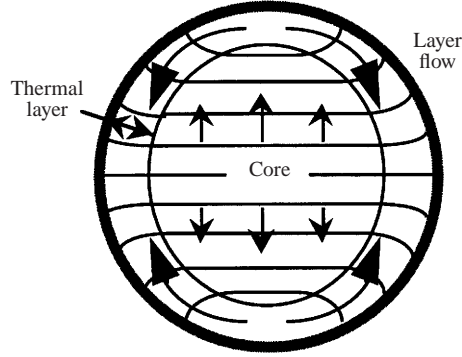
FIGURE 5. Sketch of the nearly stratified regime for $Ra_G/Ha^2 \gg 1$ (see Appendix).

The theory of the Appendix gives for the core (equations (A 10) and (A 11))

$$\Theta_s \to \frac{2}{9}\frac{Ra_G}{Ha^2}Z(3-Z^2) \quad \text{for} \quad \frac{Ra_G}{Ha^2} \gg 1,$$

in which the main qualitative difference from the first term in the expression for small Ra_G/Ha^2 given above is the independence of the result from Y (signature of stratification). The wall temperature $\Theta_s(R = 1, \alpha)$ is then found to be

$$\Theta_s(R = 1, \alpha) \to \frac{1}{9}\frac{Ra_G}{Ha^2}\sin\alpha\{5 + \cos 2\alpha\} \quad \text{for} \quad \frac{Ra_G}{Ha^2} \gg 1, \tag{18}$$

which gives the same numerical value for Θ_s as the first-order term in equation (17) when $\alpha = \pm 60°$ (as well as both expressions naturally giving $\Theta_s = 0$ at $\alpha = 0°$).

The net heat flux, which is conserved along the cylinder, is augmented by convection. Taking the scale for heat flux to be $\lambda \Delta T \pi r_0$, where λ is the thermal conductivity, the non-dimensional heat flux or Nusselt number is

$$Nu_G = \frac{1}{\pi}\int_0^{2\pi}\int_0^1 \left(\frac{\partial\Theta}{\partial X} - \frac{Ra_G}{Ha^2}U_X\Theta_s\right)R\,\mathrm{d}R\,\mathrm{d}\alpha, \tag{19}$$

in which we may take generally for the fully developed flow that $U_X = -2Z$ and $\partial\Theta/\partial X = 1$. The scale temperature ΔT is still being taken as Gr_0. When Θ_s is
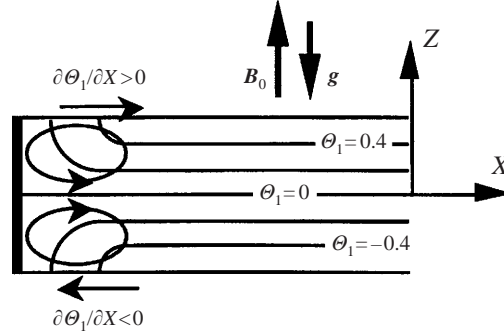
FIGURE 6. Isotherms of the first-order temperature field Θ_1 in the cold end region.

approximated by the first-order term in Ra_G/Ha^2, with Θ_1 from equation (15), we obtain for the heat flux

$$Nu_G \rightarrow \left(1 + \frac{7}{24}\left(\frac{Ra_G}{Ha^2}\right)^2\right) \quad \text{when} \quad \frac{Ra_G}{Ha^2} \rightarrow 0. \tag{20}$$

Alternatively, when we take the asymptotic $(Ra_G/Ha^2 \gg 1)$ expression for Θ_s, we obtain a remarkably similar result:

$$Nu_G \rightarrow \left(1 + \frac{5}{18}\left(\frac{Ra_G}{Ha^2}\right)^2\right) \quad \text{when} \quad \frac{Ra_G}{Ha^2} \gg 1. \tag{21}$$

At the surface of an endwall, heat flow is by conduction only. The Nusselt number Nu_G is therefore the average value of $\partial\Theta/\partial X$ there and the temperature distribution along the horizontal plane of symmetry may be expected to have the shape sketched in figure 1 for a core-driven regime in the absence of a magnetic field. An effective temperature step is formed near each endwall of the cell, but its value is dependent on the length scale over which the increased temperature gradient occurs.

2.3. *End conditions*

The question arises as to whether the cell is long enough for fully developed flow to be established. It was surmised in §2.1 for the conduction-dominated regime $(Ra_G/Ha^2 \rightarrow 0)$ that end layers of thickness order $Ha^{-1/2}$ would form on the endwalls, similar to the two-dimensional layers of Garandet *et al.* (1992). The streamlines of the fully developed shear flow (equation (11)) would then be closed within such layers and the condition for the existence of fully developed flow is that the cylindrical cell is long in comparison to the end-layer thickness, $\varepsilon \gg Ha^{-1/2}$.

When the modified Rayleigh number is small, but no longer negligible, there is vertical variation in the fully developed temperature field, which is given by equation (15) to first order in Ra_G/Ha^2. Adjustment to the constant-temperature boundary condition on the endwall is necessary and it is easily shown (Cowley 1995) that, to this order in Ra_G/Ha^2, the adjustment occurs over a length of the order of the cylinder radius. The isotherms for the perturbation temperature field are illustrated in figure 6. The end conditions force an additional perturbation to the temperature gradients in the longitudinal direction, $\partial\Theta_1/\partial X$, which in turn give rise to a buoyancy-force field with the circulations shown in figure 6. Making the assumption of a very thin endwall $Ha^{-1/2}$ layer, capable of returning both the first-order flow induced by the

buoyancy-force field and the associated longitudinal current, Cowley (1995) found that the flow would be axisymetric with a central jet away from the endwall. It is clear that for small, but not zero, Ra_G/Ha^2 the condition for fully developed flow to be established becomes $\varepsilon \ll 1$.

With Ra_G/Ha^2 larger and convection becoming more significant, the heat-flux equations (20) and (21) imply strong temperature gradients at the endwalls and the possibility arises that electromagnetic forces will no long be sufficient to balance the rotational part of the buoyancy forces there. A conventional layer with a balance between buoyancy and inertia has a thickness $O(Ra\,Pr)^{-1/4}$ and it is noteworthy that this becomes comparable with the thickness of the MHD parallel layer when $(Ra\,Pr)^{-1/4}$ is of order $Ha^{-1/2}$, which may be equivalently written $Ra/Ha^2 \sim Pr^{-1}$. A complete theory for the influence of the endwall region is not available for high levels of Ra/Ha^2, but it is clear that it could be controlling one.

3. MASCOT experimental set-up

This section describes the design of the MASCOT experimental set-up and the specific procedures especially adopted to achieve reliable measurements of temperature and electric potential. As will be found in § 4, a demanding level of accuracy is required if results are to be meaningful.

3.1. *Global description*

The basic element of the MASCOT experiment is a mercury-filled cylindrical cell (radius $r_0 = 20$ mm, length $l = 400$ mm), made of glass and equipped with sensors to measure both temperature and electric potential at the cylindrical wall.

Two thick copper disks are located at the ends of the cell whose temperatures T_1 (cold end) and T_2 (hot end) are controlled with a precision of ± 0.01 K. Such an accuracy in uniformity is achieved by careful control of water circuits providing flow to passages within the copper disks. These passages, which have the appearance of spiral labyrinths are designed so that water first flows inwards and then outwards. Moreover, three commercial temperature regulators, distributed along the water circuit stabilize temperatures to better than 10^{-3} K variation in time.

In order to minimize any unwelcome radial thermal flux, a thick coating of thermally insulating material surrounds the cell and the coating is in turn surrounded by a thick copper tube, which is in thermal contact with the two end disks.

The temperature distribution in the copper tube will correspond to an approximately uniform temperature gradient G_0 between the two endwalls. Since for the conduction-dominated regime, this is the same longitudinal gradient as in the mercury, radial heat flux for that regime is minimized. When convection becomes significant and there are 'temperature steps' at the endwalls in the mercury (ΔS_1 and ΔS_2), there is no longer a radial match in temperature between the mercury and the copper tube along the whole length, but equality remains at the endwalls and at the central transverse plane of the cell. The axial thermal flux in the tube remains uniform to within 1% along its length, as has been demonstrated by numerical simulation.

The cell is placed horizontally between the two poles of a magnet which provides a DC vertical magnetic field $\boldsymbol{B}_0$ (of intensity up to 0.613 T). Spatial uniformity of $\boldsymbol{B}_0$ has been assessed, measuring the vertical component B_z. Some departures from uniformity may be detected near the ends of the experimental set-up but they are never more than $\pm 0.9\%$. Taking account of the stability in time of the generator which supplies the electromagnet with DC current, we consider $\boldsymbol{B}_0$ to be imposed

(*a*)

(*b*)
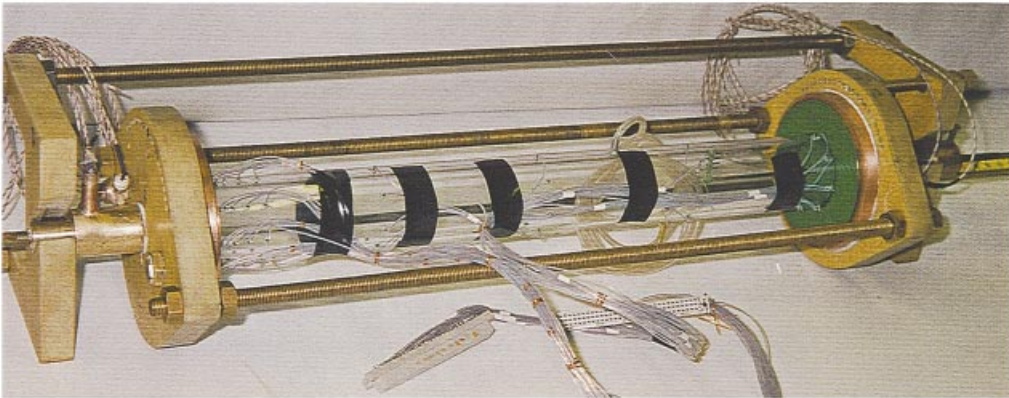
FIGURE 7. (*a*) The cell with the upper half of the thermally insulating coating and outer copper tube raised. (*b*) The cell with insulation removed.

with an absolute precision of $\pm 0.4 \times 10^{-3}$ T over one week. An extremely fine (a few μm) teflon coating on the end disks provides electrical insulation from the mercury with minimal hindrance to heat flow. Its green colour is visible in the photograph of figure 7(*b*).

Temperature conditions and level of magnetic field are fully controlled by a computer, which is also used for data acquisition. Figure 7(*a*) shows the cell with the thermally insulating coating and half of the outer copper tube raised, while figure 7(*b*) shows the cell without any insulation.

3.2. *The temperature and electric potential sensors*

Fifty-five dual-purpose sensors, capable of performing both temperature and electric potential measurements, were located at the cylindrical wall. They may be seen on the photograph of the cell given in figure 7(*b*) with copper tube and thermal insulation removed. The wall sensors are distributed on eleven half-circles, of which six are concentrated near the cold end at $x = 2, 5, 8, 12, 20$ and $30\,\mathrm{mm}$ from that end
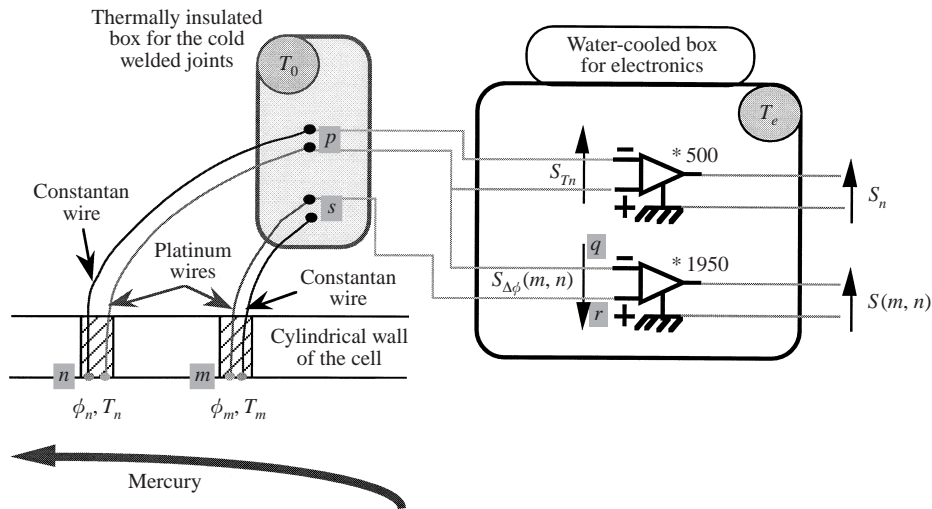
FIGURE 8. Sensors and the system for the simultaneous measurement of
temperature and electric potential.

(left-hand side of the photograph). Three other half-circles are distributed along the central region ($x = 100, 200, 300$ mm) in order to investigate the core of the flow. The last two half-circles are located in the vicinity of the hot endwall ($x = 395$, 398 mm) in order to check whether there is centro-symmetry in the temperature and electric-potential fields. By centro-symmetry we mean in the case of temperature, $T(X, Y) - T_0 = T_0 - T(-X, -Y)$, where T_0 denotes the temperature at the centre of the cell (see also equations (26) in §5). Each half-circle has five sensors located at angles $\alpha = 0°, \pm 45°, \pm 90°$, measured from the horizontal mid-plane XY (see figure 2). In addition, the cell may be rotated (see the locking screw for angular position of the cell on the right hand-side of the photograph) so that measurements may be taken at other angular positions.

The sensors act as platinum–constantan thermocouples, although electrical contact between the wires is via the mercury (figure 8). All cold welded joints of the thermocouple part of these sensors are gathered inside a box whose temperature T_0 is controlled with an accuracy of ± 0.01 K. The wires are carefully and closely set, so that after a smooth polishing of the inner glass wall, their heads just skim the mercury surface. To achieve a good electric contact with the mercury, a very thin layer of silver is electrochemically deposited onto the heads of the wires. The filling of the cell with mercury takes place under a pressure-driven flow of argon in order to avoid as much as possible any chemical impurities. As soon as contact between a sensor and mercury occurs, the formation of a mercury–silver amalgam ensures good electrical contact. The platinum wires are used also for the measurement of potential difference between pairs of sensors.

In addition to the wall sensors, five more are mounted on a movable carriage whose axial and angular position can be varied when introduced into the cell of the experiments. The five sensors are arranged along a radius arm, one being on the centreline of the cell (see figure 9) and the rod controlling the probe position is passed through the hot endwall of the cell. The presence of a movable probe within the flow introduces electrical and mechanical disturbances. However, the principal use of the probe has been to check the expected centro-symmetry both for the temperature and
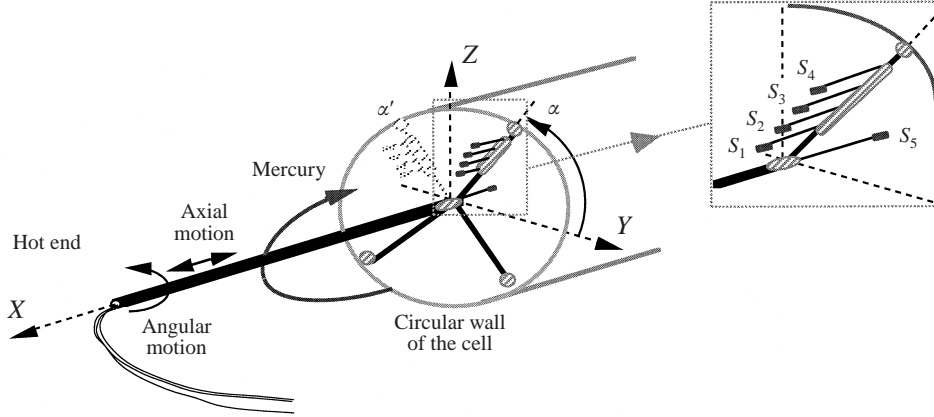
FIGURE 9. A sketch of the movable probe.

electric-potential fields. And measurements have been taken at Hartmann numbers typically in the region of 100. At this level of *Ha*, the characteristic velocity scale is of the order of $1 \, \text{mm s}^{-1}$ and the Reynolds number, based on the typical cross-sectional length scale of an element of the probe (2 mm), is less than 10. Of particular concern are the perturbation of the electric-current paths and the formation of 'wakes' aligned with the magnetic field. However, it is to be noted that the first-order current distribution (equation (10)) takes the form of circular current paths and the axial rod of the probe will have minimal influence on this current flow. The scale for the length of the 'wakes' is of order $Ha^{1/2}$ times probe thickness (i.e. 20 mm). The 'wake effect' could be more serious than the interference with current paths but the positioning of the movable carriage ($\alpha = 45°$, 135°) was such that major interference between any wakes and the sensors themselves was minimized.

As usual in the experimental investigation of MHD flows (Hunt & Shercliff 1974; Nguyen Duc & Sommeria 1988), measurement of the electric-potential difference between two points *m* and *n* is a worthwhile indicator of behaviour. Here, the problem is that the electric potential differences due to the MHD bulk flow are so weak (10^{-7}–10^{-6} V) that a non-negligible thermoelectric part contributes to the subsequent electric signal $S_{\Delta\phi}(m, n)$ between *m* and *n*. The expression for $S_{\Delta\phi}(m, n)$ follows from Ohm's law with thermoelectric term included (Shercliff 1979),

$$\boldsymbol{j}/\sigma = -\nabla\phi + \boldsymbol{u} \times \boldsymbol{B}_0 - P_{mat}\nabla T,$$

where P_{mat} denotes the absolute thermoelectric power of the various media involved in each of the elementary segments of the electrical circuit [*m–n*], [*n–p*], [*p–q*], [*q–r*], [*r–s*] and [*s–m*] (see figure 8), each of them contributing to $S_{\Delta\phi}(m, n)$. If $[\phi_n - \phi_m]_{MHD}$ represents the electric-potential difference due to the MHD bulk flow, integration of Ohm's law along the path *n-p-q-r-s-m* provides an expression for the electric signal to be amplified and measured:

$$S_{\Delta\phi}(m, n) = P_{Pt/Hg}(T_m - T_n) + (\phi_m - \phi_n)_{MHD}.$$

The symbol $P_{Pt/Hg}$ is the thermoelectric power of platinum with respect to mercury. The analogue amplifier delivers a signal,

$$S(m, n) = A(m, n) \, S_{\Delta\phi}(m, n) + \text{Offset}(m, n), \tag{22a}$$

where $A(m,n)$ and Offset(m,n) designate, respectively, the electronic gain (1950 with a precision of $\pm 5\%$) and an offset, which is slightly dependent on time.

Similar algebra leads easily to an equivalent expression for the temperature signal S_n, also at output from an analogue amplifier,

$$S_n = A_n[P_{Pt/Constantan}(T_n - T_0)] + \text{Offset}(n), \qquad (22b)$$

where the symbols A_n, $P_{Pt/constantan}$ and Offset(n) denote the gain (500 with a precision of $\pm 5\%$), the thermoelectric power of platinum with respect to constantan, which is well-known and effectively constant over the range of temperature involved, and the offset of the amplifier. To take account of the observed drift with time of either Offset(n) or Offset(m,n), measurements of $S(m,n)$, S_n, Offset(m,n) and Offset(n), were taken in succession systematically and the actual values of Offset(m,n) and Offset(n) were subtracted from signals $S(m,n)$, S_n.

Since the thermoelectric contribution to the electric signal $S(m,n)$, $P_{Pt/Hg}(T_m - T_n)$, is of the same order as the MHD contribution $[\phi_m - \phi_n]_{MHD}$, accurate knowledge of the thermoelectric power $P_{Pt/Hg}$ is essential for measurement between sensors at different temperatures. However, the experimental data on $P_{Pt/Hg}$ are not extensive (Marwaha & Cusack 1965), although they indicate both a strong variation with respect to temperature (in comparison with other liquid metals, such as gallium or tin) and a dramatic sensitivity to any traces of chemical impurities. In practice, we encountered significant problems when measuring the MHD contribution $[\phi_m - \phi_n]_{MHD}$ with a reproducibility which we could regard as satisfactory and, therefore, a restricted set of measurements was taken for the potential difference between points where the temperature is the same, thus eliminating the unwelcome thermoelectric contribution. The expected symmetry about the vertical, longitudinal, mid-plane (X, Z) implies that this temperature condition will hold between points at angles α and $180° - \alpha$ to the horizontal within each cross-section and at the same radial position. This assumption was checked by direct measurement of the temperature. Then the wall sensors were used to determine mainly the potential differences for $\alpha = 45°$ (in the upper half of the cell and along its length) in accordance with the simplified relation

$$[\phi_m(45°) - \phi_n(135°)]_{MHD} = \frac{S(m,n) - \text{Offset}(m,n)}{A(m,n)}.$$

In addition to the centro-symmetry in temperature, referred to above, a similar centro-symmetry in the electric potential field is to be expected. This was checked by measurements taken with the wall sensors and also using the movable probe. In the case of the latter, it is not possible to measure directly the difference $[\phi_m(\alpha) - \phi_n(180° - \alpha)]_{MHD}$ since the sensors are mounted on a single radius arm. The procedure adopted was to take a measurement at angle α for the potential difference between the sensor at the point of interest (position m) and the sensor which is mounted on the axis of the probe (S_5 – figure 9), which we can denote as $S(m, 5)$. The probe was then rotated to angle $\alpha' = (180° - \alpha)$ and a measurement of the potential difference $S(m', 5)$ taken at the new position (position m'). Provided that the time interval between these two measurements is sufficiently short, the drift in the offset of the single amplifier used is negligible, Offset$(m, 5)$ is same as Offset$(m', 5)$, and the difference between the measurements yields

$$[\phi_m(\alpha) - \phi_{m'}f(180° - \alpha)]_{MHD} = \frac{S(m, 5) - S(m', 5)}{A(m, 5)}.$$
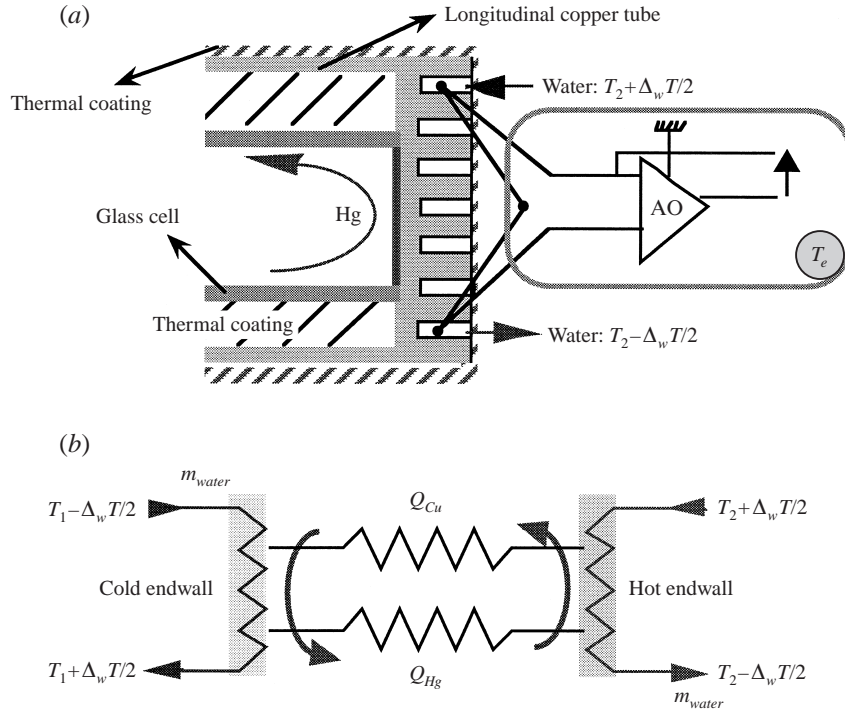
FIGURE 10. (*a*) The differential measurement of $\Delta_w T$. (*b*) Heat transfers across the cell.

3.3. *Heat transfer measurement*

As a global diagnostic of the flow, it is worth evaluating the transfer of heat from the hot endwall to the opposite cold endwall. In the present work, the Nusselt number, as defined for equations (20) and (21), can be experimentally measured as follows. Since a flow of water is used to control the temperatures T_1 and T_2 of the endwalls, the level of heat transfer is related to the temperature change $\Delta_w T$ of the water. This change (a temperature rise at the cold endwall, a temperature decrease at the hot endwall, normally of order 0.01 K) was increased to order 0.1 K by reducing the flow rate of water and could be recorded with a differential thermocouple (figure 10*a*).

The total heat flux Q_{tot} across the cell (via the mercury and the copper tube – see figures 10*a* and 10*b*) is easily calculated from $\Delta_w T$ and measurement of the water rate of flow $\dot{m}_{water}$, as the quantity $c \dot{m}_{water} \Delta_w T$, where c is the heat capacity. The same water circuit was used for the cold end and for the hot end so that $\dot{m}_{water}$ is the same for each. Assuming radial heat flux to remain weak, and this assumption is validated by the fact that temperature rise and temperature decrease $\Delta_w T$ are found to be the same, the total heat flux Q_{tot} is equal to the sum of the purely diffusive heat flux Q_{Cu} going through the cylindrical copper wall and the heat flux Q_{Hg} through the mercury, both of which may be taken as constant along the length of the cell.

Suppose now that Q_{Hg}^0 and Q_{tot}^0 refer to values taken by the heat fluxes when the imposed magnetic field $\boldsymbol{B}_0$ is at its maximum value (0.6135 T). At this condition, the regime can be assumed to be conduction dominated so that Q_{Hg}^0 is equal to $\pi r_0^2 \lambda (T_2 - T_1)/l$. Defining the Nusselt number as the ratio of the actual flux in the cell to the heat flux which would occur by pure conduction for the same overall temperature difference, and assuming that Q_{Cu} is independent of the level of the

Density ρ (kg m^{-3})	13579
Coefficient of thermal expansion β (K^{-1})	1.81×10^{-4}
Kinematic viscosity v (m^2 s^{-1})	1.04×10^{-7}
Thermal conductivity λ (W m^{-1} K^{-1})	8.69
Thermal diffusivity α_d (m^2 s^{-1})	46.06×10^{-7}
Specific heat capacity C_p (m^2 s^{-2} K^{-1})	139.4
Electrical conductivity σ (kg m s^{-3} V^{-2})	1.04×10^6

TABLE 1. Thermophysical properties of mercury at 293 K.

magnetic field, we obtain

$$Nu = \frac{Q_{Hg}}{Q_{Hg}^0} = \frac{Q_{tot} - Q_{tot}^0}{\pi r_0^2 \lambda (T_2 - T_1)/l} + 1. \tag{23a}$$

Note that the Nusselt number Nu_G, for which theoretical values were given in equations (20) and (21), has heat flux referred to conduction at the temperature gradient G of the fully developed condition, so that the prediction for Nu is given by

$$Nu = \frac{G}{(T_2 - T_1)/\ell} Nu_G. \tag{23b}$$

3.4. *Experimental uncertainties*

Thermophysical data on the molecular viscosity, volumetric expansion coefficient, electric conductivity, thermal conductivity, thermal diffusivity, and the heat capacity of mercury, depend on temperature. The values are taken at 293 K (table 1) and this implies at most relative errors of

$$\frac{\delta v}{v} \approx \pm 2\%, \quad \frac{\delta \beta}{\beta} \approx \pm 0.01\%, \quad \frac{\delta \rho}{\rho} \approx \pm 0.09\%, \quad \frac{\delta \sigma}{\sigma} \approx \pm 0.5\%,$$

$$\frac{\delta \lambda}{\lambda} \approx \pm 1.3\%, \quad \frac{\delta \alpha_d}{\alpha_d} \approx \pm 1.5\%, \quad \frac{\delta C_p}{C_p} \approx \pm 0.12\%.$$

The electromagnet provides a very steady magnetic field $\boldsymbol{B}_0$, with a spatial uniformity of $\pm 0.9\%$, and exhibits a weak hysteresis which is compensated for as much as possible. The magnetic field $\boldsymbol{B}_0$ is assessed to be controlled with an accuracy of $\delta B_0/B_0 \approx \pm 1.2\%$. By way of illustrating the difficulty experienced in measuring electric potentials, we record that this had to be done at night: broad-band noise during day time was found to be too great. Because sources of error in the amplification and data acquisition stages are complex, it is not possible to give a precise estimate of their magnitude, but it was found that the limits on reproducibility of the temperature and electric potential measurements were: $\delta(T - T_0)/(T - T_0) \approx \delta G/G \approx \pm 2\%$ and $\delta\phi/\phi \approx \pm 5\%$. Where error bars are shown on the graphs reproduced in the next sections, they are based on these figures. The relative errors in the non-dimensional numbers are estimated as $\delta Ha/Ha \approx \pm 2.5\%$, and $\delta Ra_G/Ra_G \approx \pm 4.1\%$.

In relation to the heat transfer measurements, equation (23a) yields

$$\frac{\delta Nu}{Nu - 1} = \left| \frac{\delta(Q_{tot} - Q_{tot}^0)}{Q_{tot} - Q_{tot}^0} \right| + \left| \frac{\delta \lambda}{\lambda} \right| + \left| \frac{\delta(T_2 - T_1)}{T_2 - T_1} \right|.$$
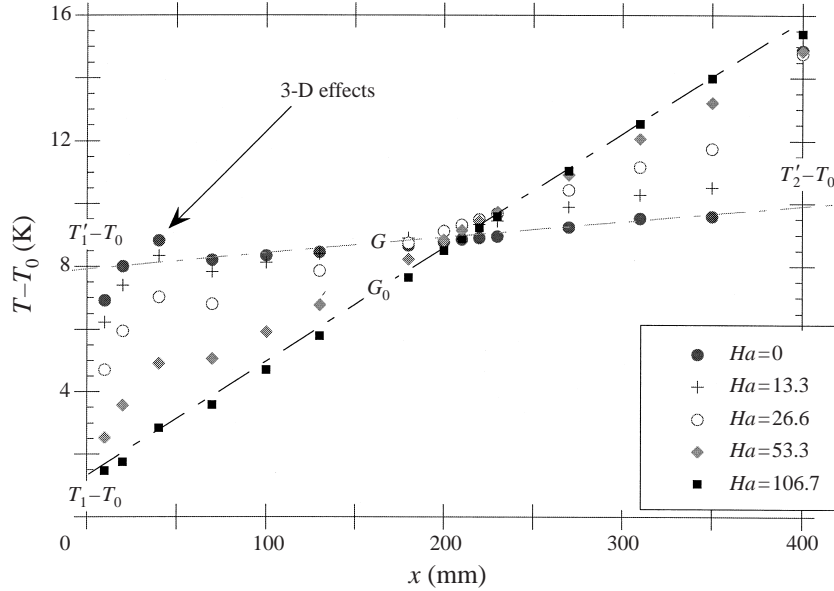
FIGURE 11. Temperature distribution $T_{45°}(x)$; the Rayleigh number ($Ra = 22.6 \times 10^3$) is based on the overall temperature difference $T_2 - T_1$.

Since Q_{tot} is derived from the measurement of the very small temperature difference $\Delta_w T$ between inlet and outlet of the water flowing through each disk, the dominant influence on δNu is

$$\delta Nu \approx \pm (Nu - 1) \left(\left| \frac{\delta(|\Delta_w T| + |\Delta_w^0 T|)}{|\Delta_w T - \Delta_w^0 T|} \right| \right),$$

neglecting the less significant errors in λ and c (water heat capacity) and any difference in $\dot{m}_{water}$ between the runs for Q_{tot} and Q_{tot}^0. Thus, for conditions such that $Nu = 1.5$, $\Delta_w T$ and $\Delta_w^0 T$ were measured as 0.1 ± 0.001 K and 0.09 ± 0.001 K whereas $\delta \dot{m}_{water}/\dot{m}_{water}$ and $\delta(T_2 - T_1)/T_2 - T_1$ were measured as $\pm 1\%$ and $\pm 2.5\%$, giving $Nu = 1.5 \pm 0.1$.

4. General features of the flow, as observed

The features observed on the temperature distributions measured at the wall of the cell are now described. Some data on temperature, which are exhibited on the following plots, are time-averaged; this holds when Ha was lower than 10 and, as time-dependent traces showed, the flow was found to be turbulent. The symbol $T_\alpha(x)$ denotes the x-dependence of temperature along the generatrix located at the angular position α, whereas $T_x(\alpha)$ designates the temperature distribution around a circle located at a particular axial position. The dimensional coordinate x is measured in millimetres from the cold endwall.

4.1. *Temperature distributions along the cylindrical wall*

On figure 11, experimental curves $T_{45°}(x)$ are plotted for an overall temperature difference $T_2 - T_1 = 14.7$ K, and various values of the Hartmann number. In each case, there is clearly a core region where the axial temperature gradient is uniform
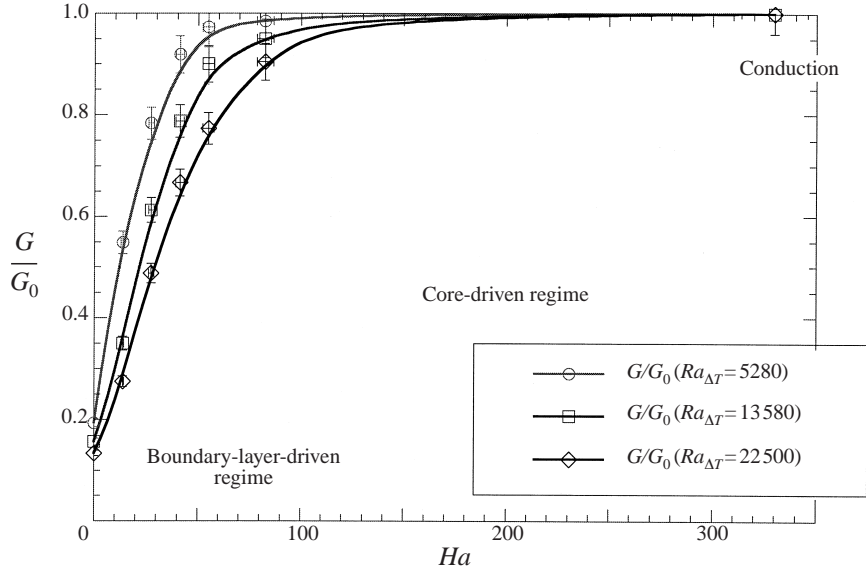
FIGURE 12. Non-dimensional axial temperature gradient G/G_0 in the core. Rayleigh numbers are based on the overall temperature difference $T_2 - T_1$. The lines represent merely an empirical fit to the data.

(denoted G), but the value varies strongly with Hartmann number. The ratio G/G_0, where $G_0 = T_2 - T_1/l$, is then seen to be a convenient indicator of the convection level. As expected, the transition from a boundary-layer-driven regime to a core-driven regime is consistent with Hartmann numbers becoming greater and also with Rayleigh numbers (or Grashof numbers) becoming smaller (figure 12). The transition between the thermal regimes is also illustrated on figure 11 by the decrease of the effective temperature steps at the endwalls, also indicated on figure 1 by ΔS_1 and ΔS_2. By temperature step, we mean the difference between the temperature which would be found at an endwall if the linear core variation were to be extended up to the wall (T_1' on figure 11) and the actual temperature, i.e. $\Delta S_1 = (T_1' - T_1)$. Note that $G = G_0 - (\Delta S_1 + \Delta S_2)/l$. The ratio G/G_0 itself acts as a criterion for the occurrence of a transition since beyond some value in the region of 0.5, the core temperature gradient G contributes primarily to the establishment of the overall temperature difference. Whatever the Grashof number, as soon as Ha is significantly larger than 100, any differene between G and G_0 no longer holds, and the regime tends to conduction domination.

As expected, it was found that there is centro-symmetry in the temperature distribution. Thus $T_{225°}(x)$ may be deduced from the results of figure 11 by $T_{225°}(X, Y, Z) = T_1 + T_2 - T_{45°}(-X, -Y, -Z)$ since $\frac{1}{2}(T_1 + T_2)$ is the temperature at the centre point.

The presence of a temperature extremum, located at $x \sim 35$ mm on the $T_{45°}(x)$ plot, is worthy of note. Although at first surprising, such a pattern can be explained by the three-dimensional recirculating flow of the end region. Consider two fluid particles travelling either side of the top generatrix and approaching the cold end. As shown by Ben Hadid & Henry (1997) from their fully three-dimensional numerical study, each of these fluid particles, rather than remaining in a vertical plane, moves outwards while descending symmetrically with respect to the longitudinal mid-plane. Convection associated with this motion leads to an increase in temperature at vertically lower
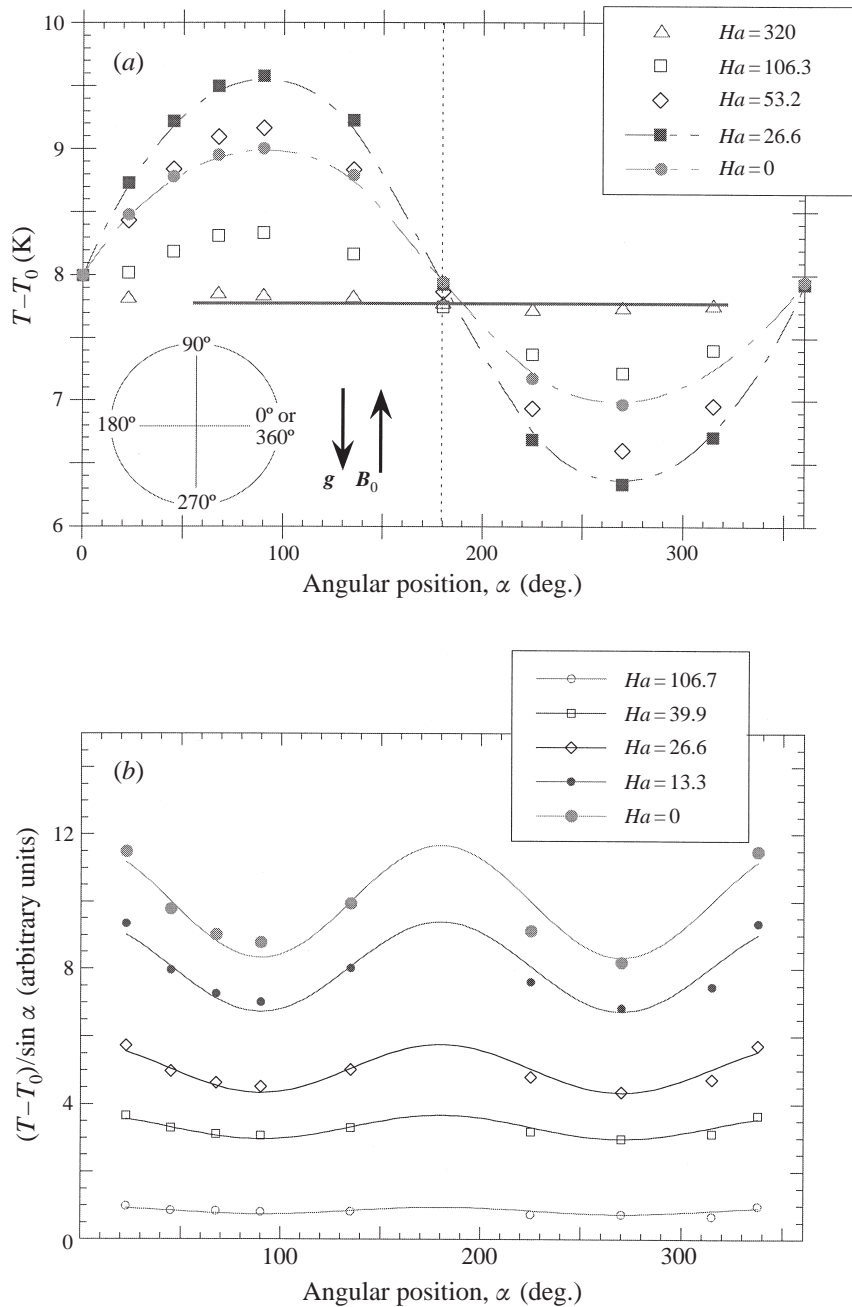
FIGURE 13. (a) Temperature distribution around the central circle at $x = 200$ mm for Ra based on the overall temperature difference 22.6×10^3. The broken lines depict best-fit-sine curves to the experimental points. (b) Measured departure from a purely sinusoidal distribution of temperature around the central circle. The lines depict best-fit curves proportional to $\cos 2\alpha$.

levels in the vicinity of the cold wall. The phenomenon is consistently observed on the generatrix at $\alpha = 45°$ when convection is significant. A symmetric extremum is also observed at $x = 365$ mm when the horizontal temperature gradient is reversed by turning the cell round: the sensors were then concentrated near the hot end.

4.2. *Temperature distribution around the central circle*

The measured temperature distribution around the central circle, $T_{200}(\alpha)$, is shown on figure 13(a). Whatever the Hartmann number, the distribution is remarkably well fitted by a sine curve whose peak-to-peak amplitude represents the maximum temperature variation over the cross-section. As expected from the MHD damping effect, the temperature becomes nearly uniform over the cross-section when the Hartmann number is high enough ($Ha > 300$), as expected for a conduction-dominated regime. But surprisingly, the amplitude first increases with increasing Hartmann number and only starts to decrease for $Ha > 26.6$. Observation of the time-dependence of measured electric potentials and temperatures indicated that the flow was undoubtedly laminar, or equivalently, that the effective viscosity was reduced to the molecular level, for $Ha > 10$ at $Ra = 22.6 \times 10^3$ (Ra here is based on the overall temperature difference). But two effects contribute to an initial increase in amplitude with increasing Hartmann number. The first is that the appropriate temperature scale is Gr_0 and the core temperature gradient increases markedly with Ha increasing (figure 12), and the second is that the high-Hartmann-number theory is not appropriate here.

The analysis of §2.2 predicted that to higher than first order in Ra_G/Ha^2 the temperature distribution around the central circle should exhibit a departure from the purely sinusoïdal form by a term proportional to $\sin \alpha \cos (2\alpha)$ (equations (17) and (18)). Although the temperature differences are small for our experimental conditions, we have enough confidence in their accuracy to reproduce results in figure 13(b) which support the prediction well.

4.3. *Core region: comparison with theory*

The data on temperature of figure 13(a) have been compared with the predictions of equations (17) and (18) in the following way. Using the method of least squares, the best fit to the mean value of $\Theta_s/\sin \alpha$ at $R = 1$ has been evaluated (coefficient of the first harmonic of the temperature distribution around the central circle) and to a $\cos 2\alpha$ law for its variation (coefficient of the second harmonic). According to equation (17), the mean value of $\Theta_s/\sin \alpha$ should vary with sufficiently low values of the modified Rayleigh number, as $0.5\,Ra_G/Ha^2 + (7/5850)(Ra_G/Ha^2)^3$, and with sufficiently high values as $(\frac{5}{9})Ra_G/Ha^2$ (equation (18)). On figure 14, the mean value of $\Theta_s/\sin \alpha$ is plotted against Ra_G/Ha^2, the values of the temperature gradient G being taken from experimental measurements (as in figure 12). It will be seen that as Ra_G/Ha^2 increases, the experimental points lie progressively further below the theoretical predictions, but the right-hand side of the plot also represents low values of Hartmann number for which the asymptotic theory developed in the Appendix will not be valid.

Also shown on figure 14 are the experimental points for the amplitude of the variation of $\Theta_s/\sin \alpha$, taken from the measurements of figure 13(b). This variation is, as expected, much smaller than the mean value. Although the points do not follow closely the scaling laws of equations (17) and (18) (i.e. that $\Theta_s/\sin \alpha$ has a $\cos 2\alpha$ dependence proportional to, respectively, $(Ra_G/Ha^2)^3$ and (Ra_G/Ha^2)), there is some indication that the level of variation is in better accordance with equation (17) as soon as Ra_G/Ha^2 is lower than 2.

In §2.2 it was explained that in a fully developed region the primary flow is not affected by the secondary transverse flow and, as mentioned in connection with equation (14), it is easily shown that there is no electric-potential field associated with the latter. It follows that, provided the Hartmann number is high enough,
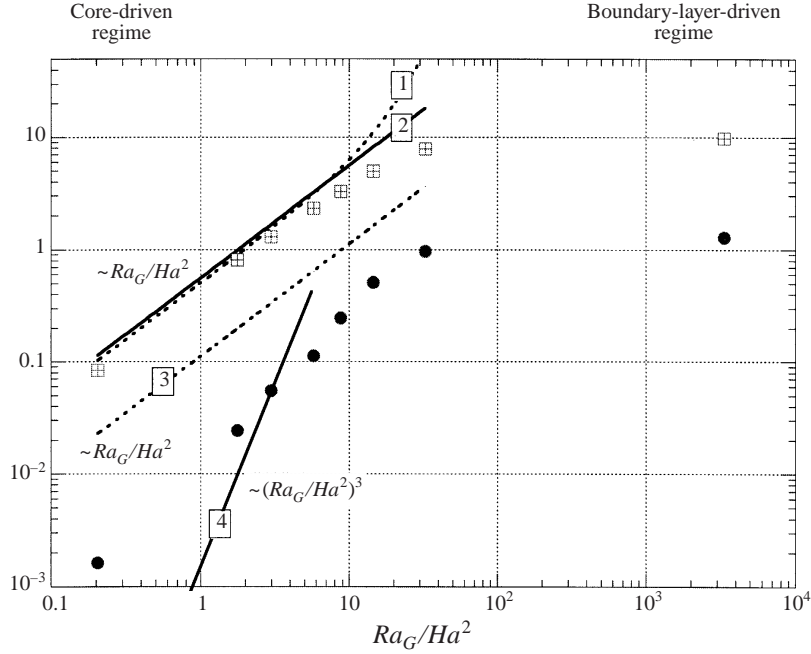
FIGURE 14. Comparison of experimentally measured values of transverse temperature variation with the predictions of theory: ⊞, mean value of $\Theta_s/\sin\alpha$ at the wall; - - - -[1]- - - -, mean value of $\Theta_s/\sin\alpha$ from equation (17); ——[2]——, mean value of $\Theta_s/\sin\alpha$ from equation (18); ●, amplitude of $\Theta_s/\sin\alpha$; - - - -[3]- - - -, amplitude of $\Theta_s/\sin\alpha$ from equation (17); ——[4]——, amplitude of $\Theta_s/\sin\alpha$ from equation (18). Ra based on the overall temperature difference $= 22.6 \times 10^3$.

equation (11) gives the potential distribution. In particular, the non-dimensional potential difference between points on the wall at angular positions $\alpha = 45°$ and $\alpha = 135° (Z = 1/\sqrt{2}, Y = \pm 1/\sqrt{2})$ is predicted to be precisely unity, i.e. the measured voltage difference $(\phi_m(45°) - \phi_m(135°))_{MHD}$ will be $u_0 B_0 r_0$, where u_0 is the scale velocity (recall that $u_0 = \rho g \beta \Delta T/(\sigma B_0^2)$ and $\Delta T = G r_0$). Note that the actual velocity at this vertical position is not equal to u_0 and some of the voltage difference is associated with resistance to electric current flowing in the Y-direction.

On figure 15, values of the measured potential difference divided by $B_0 r_0$ are plotted against the Hartmann number and then compared with the scale velocity adopted for the high-Hartmann-number theory. In calculating ΔT and consequently u_0, experimental values of G have been used. Note that the scale velocity is by definition proportional to $1/B_0^2$ (or Ha^{-2}) if G can be taken as independent of B_0 (i.e. Hartmann number high enough for a conduction-dominated regime, $G = G_0$). The agreement for $Ha > 40$ is very good, in spite of the smallness of the velocities, as indicated by the scale of the axis. Despite the difference between the values of the aspect ratios, as far as the fully developed flow is concerned good agreement with the numerical calculations by Ben Hadid & Henry (1996) is also achieved in regard to the velocity scale. At lower values of Ha, the potential measurement still provides some indication of velocity scales.

4.4. Global heat transfer

As described in §3.3, measurement of the small temperature change in the temperature-controlling water flows to the endwalls provided a means of deducing net heat flux
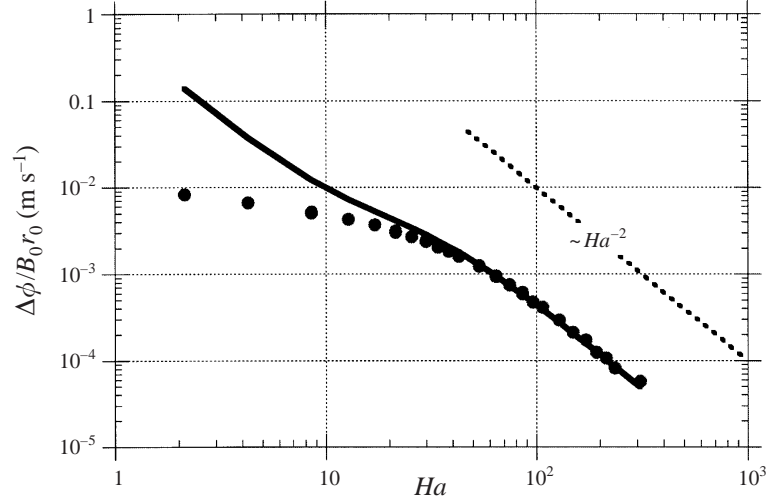
FIGURE 15. Electric-potential difference between sensors located at $\alpha = 45°$ and $\alpha = 135°$ in units of scale velocity: ●, measured points at $Ra = 22.6 \times 10^3$; —, velocity scale u_0; ····, slope for Ha^{-2} dependence.
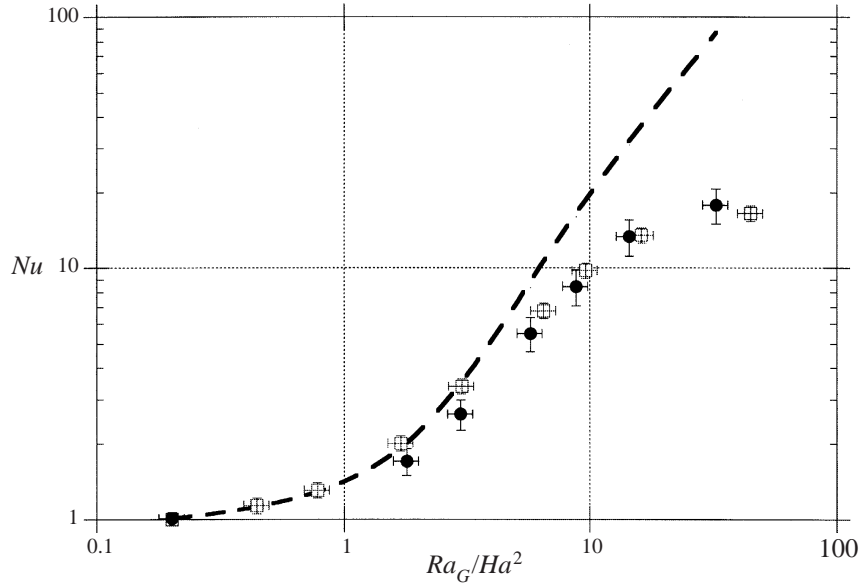
FIGURE 16. Heat transfer across the cell for an overall Rayleigh number of $Ra = 22.6 \times 10^3$: ⊞, Nusselt number derived from measured rate of overall heat transfer (equation (23a)); ●, Nusselt number derived from temperature and electric potential measured at the central plane, together with interpolated values of G (equation (25) with (23b)); - - -, theoretical prediction using interpolated values of G (equations (20) and (21) with (23b)).

through the mercury cell. Values of Nusselt number found in this way are plotted on figure 16. For comparison, the prediction of the analysis for fully developed flow (equation (20) for low values of Ra_G/Ha^2 and equation (21) for high values) is represented by a single line since on the scale of the graph the difference between the two equations is negligible. In making this comparison, values of the temperature gradient G in the fully developed region have been interpolated from measured values, such

as those presented on figure 12, so that Nu may be related to Nu_G in accordance with equation (23b). It will be seen that there is good agreement between measurement and prediction up to values of Ra_G/Ha^2 in the region of 2, corresponding to a Hartmann number of 80.

An interesting empirical result has been found to hold over the whole range of modified Rayleigh number Ra_G/Ha^2. To derive the result, it is assumed first that the shape of the temperature distribution over the central cross-section is adequately given by the theory for low values of Ra_G/Ha^2 (equation (15)), but the magnitude of the overall temperature difference is taken from measurement, i.e.

$$T(\alpha) = T(0°) + \tfrac{1}{4}[T(90°) - T(270°)]R(3 - R^2)\sin\alpha. \tag{24a}$$

Second, it is assumed that the longitudinal velocity has the linear distribution with Z of equation (10), while the scale velocity is given by the difference in electric-potential behaviour at points $\alpha = 45°$ and $\alpha = 135°$, i.e.

$$u = -2Z[\phi(45°) - \phi(135°)]/(B_0 r_0). \tag{24b}$$

Integration for the net heat flux then yields

$$Nu_G = 1 + \frac{7}{24}\frac{[T(90°) - T(270°)][\phi(45°) - \phi(135°)]}{\alpha_d G B_0 r_0}. \tag{25}$$

Values of Nusselt number deduced from this equation, equation (23b) and measurement of temperature difference, potential difference and G, are included on figure 16 and remarkable agreement is achieved. This suggests that the velocity distribution represented by equation (24b) has wider validity than might otherwise be expected.

The fact that heat transfer rates exceed those for pure conduction in accordance with our chosen velocity scale is a good indication that the Hartmann layers along the cell are passive. This scale is proportional to $1/B_0^2$ (or $1/Ha^2$ in the absence of changes to length, etc.) which leads to the $(Ra_G/Ha^2)^2$ dependence found for $Nu - 1$. If the Hartmann layer were active, this scaling law for heat transfer would be expected to be closer to the form $Nu - 1 \sim Ra_G/Ha^2$. It is worthy of note that the Nusselt number may act as a convenient experimental measure of whether there is any electrical activity of the Hartmann layer.

5. Longitudinal variation

In this section, we present temperature and electric-potential measurements which provide some information on how the flow and electromagnetic conditions vary along the length of the cell. At the beginning of §4, figure 11 showed how temperature measured at $\alpha = 45°$ varied with distance x along the cylinder for various Hartmann numbers. The apparent constancy of the temperature gradient G over a substantial length was the basis for assuming fully developed conditions at the central cross-section of the cylinder. It will now be seen that the assumption is not as soundly based as might be wished, especially at low Hartmann numbers, although we believe that the conditions were near enough to fully developed for comparison with the theory of §2.2 to be reasonable.

Two general features of the measurements are worthy of immediate note. The first is that no departure was detected from symmetry about the longitudinal vertical XZ mid-plane. The second is confirmation of centro-symmetry, i.e.

$$T(X,Z) - T_0 = T_0 - T(-X,-Z), \quad \phi(X,Z) - \phi_0 = \phi_0 - \phi(-X,-Z). \tag{26}$$
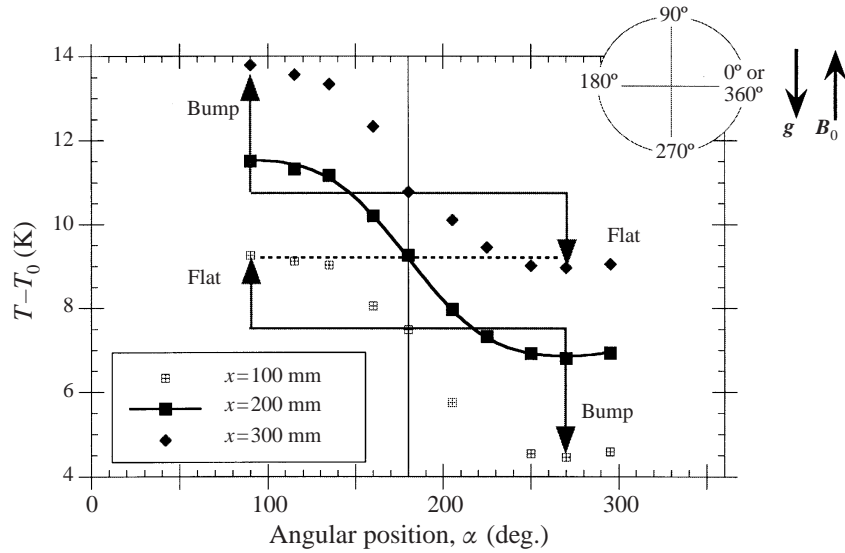
FIGURE 17. Variation of the shape of the temperature distribution around the cylinder at $x = 100$, 200 and 300 mm. The overall Rayleigh and Hartmann numbers are, respectively, 27×10^3 and 26.6.

Recall that T_0 and ϕ_0 denote temperature and electric potential at the centre point of the cell ($x = 200$ mm, $r = 0$ mm). Although detailed results are not reproduced in the following sections, this confirmation includes checks on potential differences measured by the movable probe at various radii and angular settings.

5.1. *Temperature measurements*

Figure 17 shows the distribution of temperature around the cylindrical wall at the central transverse plane and at the planes halfway between the centre and the ends of the cell, namely, $x = 200$, 100 and 300 mm from the cold end. That the symmetric form (about $\alpha = 180°$) of the temperature distribution around the central circle has been significantly distorted at the other two circles is clearly apparent.

Reference was made in §2.3 to the first-order solution in Ra_G/Ha^2 near the endwalls of the cell (Cowley 1995) adjusting to the fully developed condition over a length of the order of the cell radius r_0. Since the latter is 20 mm, it would appear that the actual length of the adjustment zone is significantly greater than r_0 under the conditions of the figure 17 measurements. Furthermore, the first-order solution is such that a sinusoidal distribution of temperature with α is maintained throughout the core, with only amplitude diminishing as the endwalls are approached.

However, it is not surprising that not even qualitative agreement with the first-order solution is being obtained since for the Hartmann number 26.6 and overall Rayleigh number 27×10^3, the ratios G/G_0 and Ra_G/Ha^2 are, respectively, 0.45 and 17.2. We suggest that the results are beginning to show evidence of transition to a regime with a thermal boundary layer on the cylindrical wall of the cell, although Ra_G/Ha^2 is not large enough for a strictly thin layer if that is the controlling parameter. Three observed features are worthy of note. The first is that the temperature distribution becomes flatter in the direction of flow, i.e. from the hot end to the cold end at $\alpha = 90°$ and from the cold end to the hot end at $\alpha = 270°$. The second is that the temperature field is approaching a condition of horizontal stratification, i.e. the temperature difference over an axial length of 200 mm at $\alpha = 90°$ is 3.2 K, while
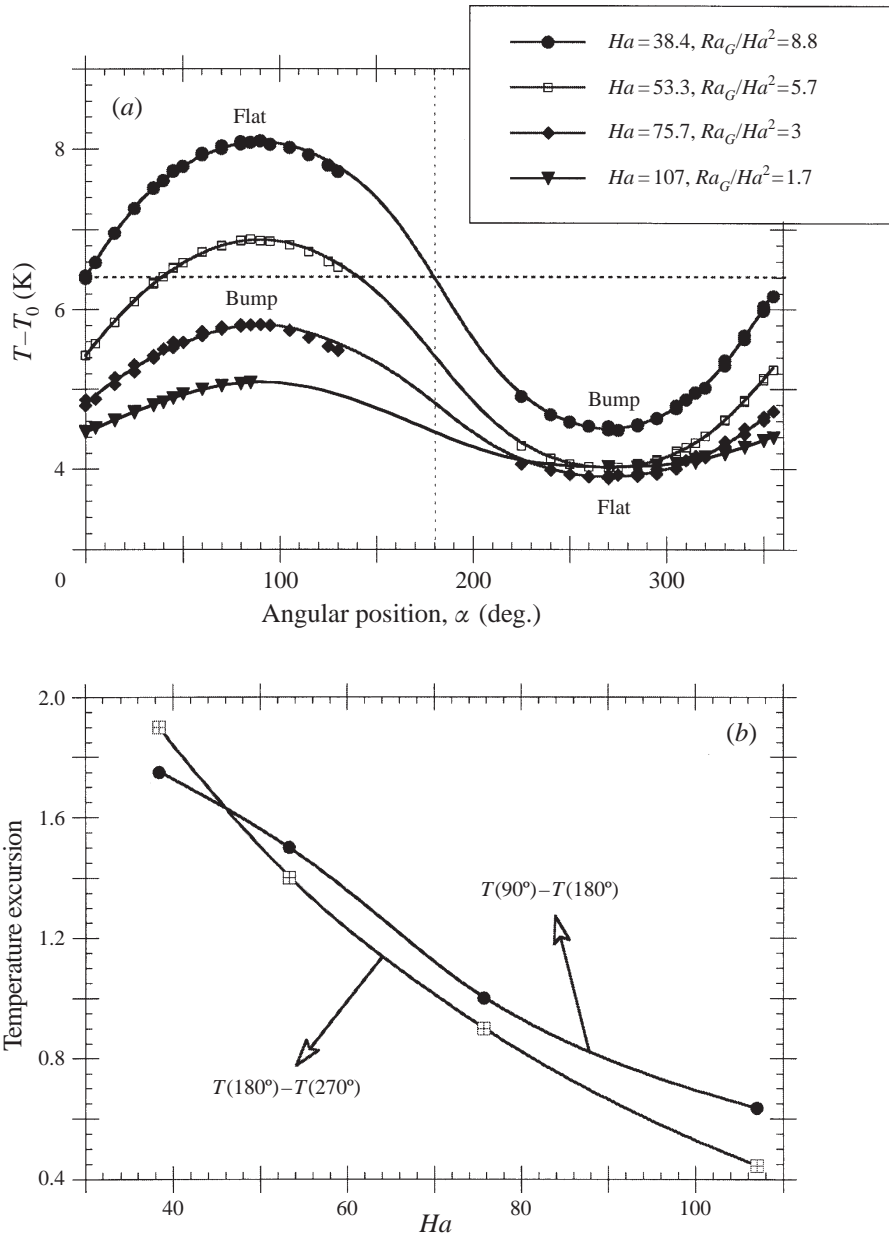
FIGURE 18. (a) The temperature distribution around the cell near the cold end ($x = 30$ mm) at low values of Ra_G/Ha^2 (overall Rayleigh number of 22.6×10^3). (b) Asymmetry of the temperature extrema.

the temperature difference over the vertical diameter of 40 mm is 4.7 K. The third point is that the case is one of substantial temperature steps near the endwalls since $G/G_0 = 0.45$ (see also figure 11). Mention was made in § 2.3 of thermal effects being likely to modify the endwall MHD layer when Ra/Ha^2 is of the order of Pr^{-1}, a criterion which is satisfied. An interesting feature is the slight reversal of the departure from symmetry as conditions settle down at high Hartmann number to a core-driven and subsequently conduction-dominated regime, as illustrated by figure 18(b), when
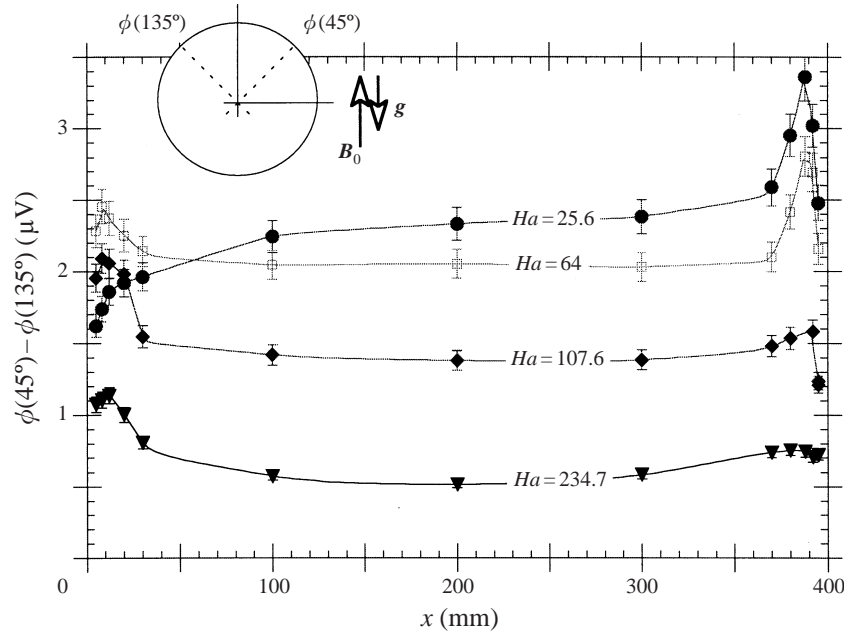
FIGURE 19. Electric-potential distribution along the upper part of the cell. Rayleigh and Grashof numbers based on the overall temperature difference $T_1 - T_2$ are, respectively, 22.6×10^3 and 8.38×10^5.

temperature distributions around the circle at $x = 30\,\mathrm{mm}$ from the cold endwall (less than one diameter) are plotted (figure 18a). As the Hartmann number is further increased, it was found experimentally that, for given overall Rayleigh number Ra, the vertical temperature distribution becomes more symmetrical about the horizontal XY mid-plane over a longer length.

5.2. *Investigation of the end flow from electric potential measurements*

Results of the measurement of electric-potential difference between $\alpha = 45°$ and $\alpha = 135°$ along the length of the cell are plotted against longitudinal position x on figure 19. Recall (see §4.3) that this measurement is equal to $u_0 B_0 r_0$, where u_0 is the scale velocity, in a fully developed region at high Hartmann number, but note also the extremely low-level voltage signal which is being recorded here.

An important feature of the potential measurements is that there is no evidence of there being any region where the level increases markedly, i.e. by a factor of the order of the Hartmann number. The situation does appear to be one where the Hartmann layers are inactive everywhere.

The measured potential differences are effectively constant over the majority of the length of the cell for given Hartmann number and within experimental accuracy; this is true even for a moderate level of Ha ($Ha = 64$). This supports the idea of a fully developed flow in the core region. Thus there is no information to be gained from this part of the curves on the approach to a core-driven regime.

What is of interest is the complex behaviour near the endwalls. There is evidence of substantial departures from symmetry about the horizontal mid-plane XY even at quite high Hartmann numbers. Recall that because of centro-symmetry, the potential difference $\phi(225°) - \phi(315°)$ at the hot end ($x = 400\,\mathrm{mm}$) may be deduced from measurement shown at the cold end ($x = 0\,\mathrm{mm}$) by means of equation (26), a point
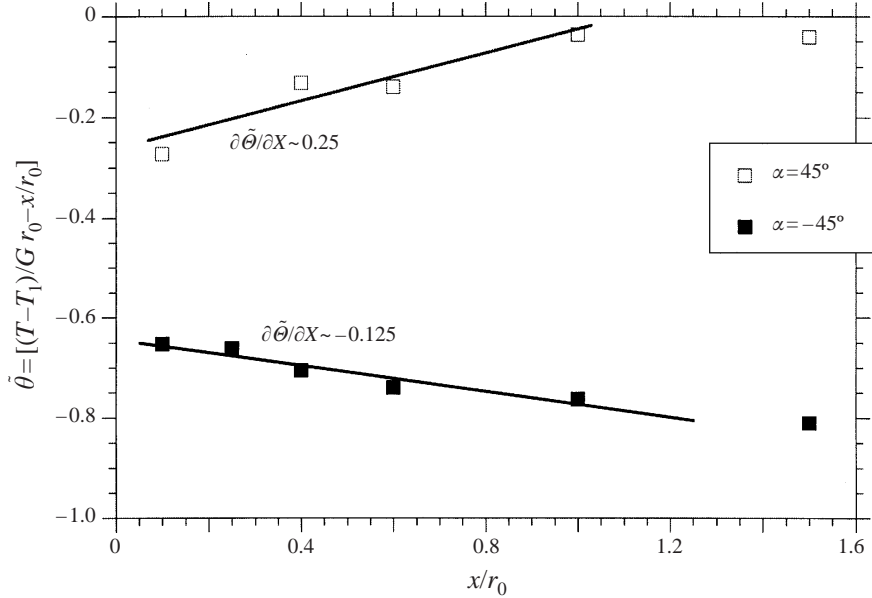
FIGURE 20. Axial temperature gradient near the cold end at two angular positions $\alpha = \pm 45°$. The Hartmann and overall Rayleigh numbers are, respectively, 107.6 and 22.6 × 10³.

which was also experimentally checked. What is clear from figure 19 is that there are substantial voltage gradients near the endwalls. When the regime is conduction dominated or core driven, the subsequent Y-component of the balance between the curls of the electromagnetic and buoyancy forces (equation (8)) is consistent with the observation of both an extremum on the electric-potential measurement near the cold endwall and the break-up of horizontal XY symmetry for the temperature distribution around circles located in the vicinity of the cold wall. This behaviour has already been made evident by the numerical calculations of Davoust *et al.* (1997). Further details of this lack of symmetry at even quite high values of Hartmann number are provided by the results plotted on figure 20 for very small distances from the cold endwall. What is represented is the departure in temperature from that of a uniform gradient G which applies in the core. At $\alpha = 45°$, the gradient of this departure is consistent with an augmentation of heat transfer rate by conduction at the wall (providing additional flux to cope with the convection in the core), but at $\alpha = -45°$, the heat transfer rate by conduction is decreased. It is possible to show from a scaling analysis based on the aforementioned balance how these temperature departures are able to drive additional voltage gradients in the Y-direction. Continuity of the electric current implies axial voltage gradients also in the end re-circulating flow since the Hartmann layer is observed to be passive.

6. Conclusion

The internal MHD thermogravitational flow studied in this paper is stabilized as soon as a Hartmann number of the order of 10 is reached (Davoust *et al.* 1995). This efficient suppression of turbulence is related to the crucial fact that, under the geometrical conditions of the flow, the Hartmann layer which develops along the longitudinal wall of the cylindrical enclosure remains electrically inactive. This hypothesis of the asymptotic analysis is confirmed by our experimental measurements.

It follows that electric-current paths are closed mainly within the core and not via the Hartmann layer. It is therefore not surprising that the two-dimensional analytical prediction of the MHD buoyancy-driven flow within the vertical longitudinal XZ mid-plane (Garandet *et al.* 1992) is close to our three-dimensional calculations both qualitatively and in order of magnitude. When the magnetic field magnitude is significantly large ($Ha \sim 100$), the MHD reorganization of the laminar flow stems from the need to balance the curl of the buoyancy force with the curl of the magnetic force. The horizontal components of this balance are thus responsible for:

a Hadley loop within vertical longitudinal XZ-planes (Y-component of the balance);

three-dimensional recirculating loops within cross-sections (X-component).

We have been able to present some experimental evidence on the nature of the transition from conduction-dominated to core-driven and then to boundary-layer-driven regimes as Ra_G/Ha^2 is increased. For conduction domination, the temperature field is even about the XY mid-plane, the axial velocity odd and other components of velocity even. With convection of temperature becoming noticeable, the perturbation to the temperature field is odd about the XY mid-plane, and transverse components of velocity even. However, as Ra_G/Ha^2 increases further, these symmetry concepts begin to lose value, as has been indicated by the measurements of temperature distribution illustrated in figure 18(*a*), the differences in electric potential illustrated in figure 19 and the axial temperature gradients of figure 20. The evidence is consistent with a strengthening thermal influence of the boundary layers on the hot and cold endwalls and a process of development in the axial direction. Of particular note are the electric-potential extrema in figure 19 in the upper half of the cell near the cold end (and correspondingly in the lower half near the hot end). These extrema were also observed in the computational work of Davoust *et al.* (1997), where they were associated with re-circulating loops at each end in addition to the main Hadley loop. These additional loops also carry a weak transverse component of vorticity $\hat{\boldsymbol{y}} \cdot (\nabla \times \boldsymbol{U})$, of the same sign as that of the Hadley loop.

In agreement with theory, asymptotic laws for the fully developed MHD core flow have been experimentally validated for velocity and convective heat transfer rates: $u_0 = \rho g \beta \Delta T / (\sigma B_0^2)$; the convective part of Nu scales as $(\pi r_0^2 \lambda \, \Delta T / L) \, (Ra_G^2 / Ha^4)$.

Little mention has been made in this paper of inertia effects. However, for any detailed treatment of the endwall layers and departure from the fully developed flow condition in the core, inertia effects will become important at moderate Hartmann numbers, the criterion being the value of $Gr^{1/2}/Ha^2$ (Lykoudis 1961).

Finally, it is worth noting that local measurements have been taken by new dual-purpose sensors specially designed to remove unwelcome thermoelectric contributions to potentials. Their technology and the associated measurement strategy have been presented in this paper.

Appendix. The fully developed secondary flow for $Ra_G/Ha^2 \to \infty$

In this Appendix we outline the model and solution which lead to equation (18) for the wall temperature distribution in a region of fully developed flow as $Ra_G/Ha^2 \to \infty$.

It turns out that the inverse of this parameter is the thickness of a thermal boundary layer which we require to be thin, while still being much thicker than the Hartmann layer. Conditions for the model are therefore $Ha^3 \gg Ra_G \gg Ha^2$. The equations governing the temperature associated with the transverse flow and governing the flow itself are (13) and (14), which are repeated here for convenience:

$$\frac{\partial^2 \Theta_s}{\partial Y^2} + \frac{\partial^2 \Theta_s}{\partial Z^2} = \frac{Ra_G}{Ha^2} \left(-2Z + U_{sy} \frac{\partial \Theta_s}{\partial Y} + U_{sz} \frac{\partial \Theta_s}{\partial Z} \right), \qquad (A\,1)$$

$$\frac{\partial^2 \Psi_s}{\partial Z^2} = \frac{\partial \Theta_s}{\partial Y}, \qquad (A\,2)$$

where the term $-2Z$ in the parentheses on the right-hand side of equation (A 1) is the contribution of the primary flow to convection, which is unaffected by the secondary flow. The balancing of the curl of the buoyancy force and the curl of the Lorentz force (equation (A 2)) can be expressed, for the latter force, directly in terms of the stream function Ψ_s because no longitudinal component of the electric field is associated with the secondary flow.

The starting point for the model is the observation that the four-vortex structure, found for the flow when Ra_G/Ha^2 is small, will tend to advect the temperature in such a way as to flatten the isotherms. If they become horizontal, the buoyancy force loses its curl. However the adiabatic boundary condition demands that the isotherms be normal to the wall and it is supposed that the necessary adjustment to their slope occurs in a thin, but inviscid, thermal layer, viscous effects being confined to an even thinner Hartmann layer. The thermal layer is of the same type as ones investigated in a study of buoyancy-driven flow in tilted containers (Cowley 1996). The temperature field is expressed as

$$\Theta_s = \Theta_c + \Theta_b,$$

where Θ_c is the core temperature, taken to be a function of Z only (horizontal isotherms), while Θ_b is the departure from that temperature in the thermal boundary layer. If thermal conduction in the core associated with the vertical variation of Θ_c is comparable with convection by the primary flow, equation (A 1) shows that Θ_c is of order Ra_G/Ha^2. Consistent with this magnitude are $\Theta_b = O(1)$, $\Psi_s = O(Ha^2/Ra_G)$ and $\partial/\partial n = O(Ra_G/Ha^2)$ where n is the inward normal at the wall. Noting that in the thermal layer the influence of the primary flow and of Θ_b may be neglected on the right-hand side of equation (A 1) and that Θ_c cannot contribute to the right-hand side of (A 2), we obtain to leading order in the layer

$$\frac{\partial^2 \Theta_b}{\partial n^2} = \frac{Ra_G}{Ha^2} \left(\frac{\partial \Psi_s}{\partial n} \cos \alpha \right) \frac{\mathrm{d}\Theta_c}{\mathrm{d}Z}, \qquad (A\,3)$$

$$\frac{\partial^2 \Psi_s}{\partial n^2} \sin^2 \alpha = \frac{\partial \Theta_b}{\partial n} \cos \alpha, \qquad (A\,4)$$

where α is the angle of the radius vector to the horizontal, as in figure 2. The boundary conditions on Θ_b and Ψ_s are

$$\frac{\partial \Theta_b}{\partial n} = \frac{\mathrm{d}\Theta_c}{\mathrm{d}Z} \sin \alpha \quad \text{at} \quad n = 0 \text{ (adiabatic wall)}, \qquad (A\,5a)$$

$$\Psi_s = 0 \quad \text{at} \quad n = 0, \qquad (A\,5b)$$

$$\Theta_b \to 0 \quad \text{as} \quad n \to \infty, \qquad (A\,5c)$$

accommodation to the no-slip condition being accomplished by the thinner Hartmann layer. The solution for Ψ_s is

$$\Psi_s = -\frac{Ha^2}{Ra_G}\left(1 - \mathrm{e}^{-kn}\right)\tan\alpha, \text{ where } k^2 = \frac{Ra_G}{Ha^2}\frac{\mathrm{d}\Theta_c}{\mathrm{d}Z}\cot^2\alpha. \qquad (A\,6a,b)$$

The information to be carried over to the core solution is the value of Ψ_s as $n \to \infty$, which we denote by

$$\Psi_o = -\left(Ha^2/Ra_G\right)\tan\alpha. \qquad (A\,7)$$

The result (A 7) has two interesting features. The first is that the stream function in dimensional terms has no dependence on the level of the magnetic field:

$$\psi_o = -\alpha_d\tan\alpha,$$

where α_d is the thermal diffusivity. The second is that the result may be derived from conservation of overall heat fluxes to a small element of the layer, but the present derivation via the layer solution (A 6a, b) is given here in order to reveal the structure of the layer.

Returning to the core, equations (A 1) and (A 2) imply that U_{sz} is constant on each horizontal isotherm and balancing the net core flow across each plane $Z = $ const. with the return flow in the thermal layer we obtain

$$U_{sz}\cos\alpha = -\Psi_o = \left(Ha^2/Ra_G\right)\tan\alpha,$$

from which it follows that the convection term associated with U_{sz} is of the same order as the contribution from the primary flow. Since $\tan\alpha = Z/\sqrt{1 - Z^2}$, the core temperature equation to leading order is finally found to be

$$\frac{\mathrm{d}^2\Theta_c}{\mathrm{d}Z^2} - \frac{Z}{1 - Z^2}\frac{\mathrm{d}\Theta_c}{\mathrm{d}Z} = -2\left(\frac{Ra_G}{Ha^2}\right)Z. \qquad (A\,8)$$

Integrating equation (A 8) once yields

$$\frac{\mathrm{d}\Theta_c}{\mathrm{d}Z} = \frac{2}{3}\frac{Ra_G}{Ha^2}(1 - Z^2) + \frac{C}{\sqrt{1 - Z^2}}, \qquad (A\,9)$$

where C is a constant of integration. Since the wall of the cylinder is adiabatic and vertical velocity on the plane $Z = 0$ is zero, the net rate of change of longitudinal enthalpy flux with X in the upper half of the cylinder must be balanced by heat conduction across $Z = 0$, i.e.

$$\frac{Ra_G}{Ha^2}\int_0^1 U_X(1 - Z^2)^{1/2}\,\mathrm{d}Z = -\left.\frac{\mathrm{d}\Theta_c}{\mathrm{d}Z}\right|_{Z=0},$$

using the fact that the longitudinal temperature gradient is unity in the non-dimensional variables and neglecting any small influence of the thermal layer on the net heat conduction. With $U_X = -2Z$ (equation (12)), the condition yields $\mathrm{d}\Theta_c/\mathrm{d}Z = \frac{2}{3}(Ra_G/Ha^2)$ at $Z = 0$ and the constant C in (A 9) must therefore be zero. Noting that Θ_c is odd in Z, integration of (A 9) gives

$$\Theta_c = \frac{2}{9}(Ra_G/Ha^2)Z(3 - Z^2), \qquad (A\,10)$$

and to leading order in the thermal layer

$$\Theta_s = \Theta_c. \qquad (A\,11)$$

Elimination of Θ_c between (A 10) and (A 11) leads to the form given as equation (18) of §2.2.

REFERENCES

ALBOUSSIÈRE, T., GARANDET, J. P. & MOREAU, R. 1993 Buoyancy driven convection with a uniform magnetic field. Part 1. Asymptotic analysis. *J. Fluid Mech.* **253**, 545–563.

ALBOUSSIÈRE, T., GARANDET, J. P. & MOREAU, R. 1996 Asymptotic analysis and symmetry in MHD convection. *Phys. Fluids* **8**, 2215–2226.

BEJAN, A. 1984 *Convection Heat Transfer*. Wiley & Sons.

BEN HADID, H. & HENRY, D. 1996 Numerical simulation of convective three-dimensional flows in a horizontal cylinder under the action of a constant magnetic field. *J. Cryst. Growth* **166**, 436–445.

BEN HADID, H. & HENRY, D. 1997 Numerical simulation of convection in the horizontal Bridgman configuration under the action of a constant magnetic field. Part II. Three-dimensional flow. *J. Fluid Mech.* **333**, 57–83.

CORMACK, D. E., LEAL, L. G. & IMBERGER, J. 1974 Natural convection in a shallow cavity with differentially heated endwalls, Part 1. Asymptotic theory. *J. Fluid Mech.* **65**, Part 2, 209–229.

COWLEY, M. D. 1995 The effect of a buoyancy-driven magnetohydrodynamic flow on the temperature distribution in a horizontal cylinder. *Magnetohydrodynamics* **31**, 227–236.

COWLEY, M. D. 1996 Natural convection in rectangular enclosures of arbitrary orientation with magnetic field vertical. *Magnetohydrodynamics* **32**, 390–398.

DAVOUST, L., MOREAU, R., BOLCATO, R., ALBOUSSIÈRE, T., NEUBRAND, A. C. & GARANDET, J. P. 1995 Influence of a vertical magnetic field on convection in the horizontal Bridgman configuration. *Magnetohydrodynamics* **31**, 218–226.

DAVOUST, L., MOREAU, R., COWLEY, M. D., TANGUY, P. A. & BERTRAND, F. 1997 Numerical and analytical modelling of the MHD buoyancy-driven flow in a Bridgman crystal growth configuration. *J. Cryst. Growth* **180**, 422–432.

GARANDET, J. P., ALBOUSSIÈRE, T. & MOREAU, R. 1992 Buoyancy driven convection in a rectangular enclosure with a transverse magnetic field. *Intl J. Heat Mass Transfer* **35**, 741–748.

HART, J. E. 1983 Low Prandtl number convection between differentially heated endwalls. *Intl J. Heat Mass Transfer* **26**, 1069–1083.

HUNT, J. C. R. & SHERCLIFF, J. A. 1974 Magnetohydrodynamics at high Hartmann number. *Ann. Rev. Fluid Mech.* **3**, 37–62.

JUEL, A., MULLIN, T., BEN HADID, H. & HENRY, D. 1998 Magnetohydrodynamic convection in molten gallium. *J. Fluid Mech.* **378**, 97–104.

LANGLOIS, W. E. 1985 Buoyancy-driven flows in crystal-growth melts. *Ann. Rev. Fluid Mech.* **17**, 191–215.

LYKOUDIS, P. S. 1961 Natural convection of an electrically conducting fluid in the presence of a magnetic field. *Intl J. Heat Mass Transfer* **5**, 23–34.

MARWAHA, A. S. & CUSACK, N. E. 1965 The absolute thermoelectric power of liquid metals. *Phys. Lett.* **22**, 556.

NEUBRAND, A. C., GARANDET, J. P., MOREAU, R. & ALBOUSSIÈRE, T. 1995 Effect of a slight non-uniformity of the magnetic field on MHD convection. *Magnetohydrodynamics* **1**, 3–18.

NGUYEN DUC, J. M. & SOMMERIA, J. 1988 Experimental characterisation of steady two-dimensional vortex couples. *J. Fluid Mech.* **192**, 175–192.

OZOE, H. & OKADA, K. 1989 The effect of the direction of an external magnetic field on the three-dimensional natural convection in a cubical enclosure. *Intl J. Heat Mass Transfer* **32**, 1939–1954.

SHERCLIFF, J. A. 1979 Thermoelectric magnetohydrodynamics. *J. Fluid Mech.* **91**, 231–246.

SOMMERIA, J. & MOREAU, R. 1982 Why, how and when MHD turbulence becomes two-dimensional? *J. Fluid Mech.* **118**, 507–518.

UTECH, H. P. & FLEMINGS, M. C. 1966 Elimination of solute banding in indium antimonide crystal growth. *J. Appl. Phys.* **37**, 2021–2023.